World Scientific
www.worldscientific.com

Bioelectrical effects of mechanical feedbacks
in a strongly coupled cardiac electro-mechanical model

Piero Colli Franzone

Department of Mathematics,
Università di Pavia,
Via Ferrata 1, 27100 Pavia, Italy
colli@imati.cnr.it

Luca F. Pavarino* and Simone Scacchi[†]

Department of Mathematics,
Università di Milano,
Via Saldini 50, 20133 Milano, Italy
**luca.pavarino@unimi.it*
[†]*simone.scacchi@unimi.it*

The aim of this work is to investigate by means of numerical simulations the effects of myocardial deformation due to muscle contraction on the bioelectrical activity of the cardiac tissue. The three-dimensional electro-mechanical model considered consists of the following four components: the quasi-static orthotropic finite elasticity equations for the deformation of the cardiac tissue; the active tension model for the intracellular calcium dynamics and cross-bridge binding; the orthotropic Bidomain model for the electrical current flow through the tissue; the membrane model of the cardiac myocyte, including stretch-activated currents (I_{SAC}). In order to properly take into account cardiac mechanical feedbacks, the electrical current flow is described in a strongly coupled framework by the Bidomain model on the deformed tissue. We then derive a novel formulation of the Bidomain model in the reference configuration, with complete mechanical feedbacks affecting not only the conductivity tensors but also a convective term depending on the velocity of the deformation. The numerical simulations are based on our finite element parallel solver, which employs both Multilevel Additive Schwarz preconditioners for the solution of linear systems arising from the discretization of the Bidomain equations and Newton–Krylov-Algebraic Multigrid methods for the solution of nonlinear systems arising from the discretization of the finite elasticity equations. The results have shown that: (i) the I_{SAC} current prolongs action potential duration (APD) of about 10–15 ms; (ii) the inclusion into the model of both I_{SAC} current and the convective term reduces the dispersion of repolarization of about 7% (from 139 to 129 ms) and increases the dispersion of APD about three times (from 13 to 45 ms). These effects indicate that

mechanical feedbacks might influence arrhythmogenic mechanisms when combined with pathological substrates.

1. Introduction

The spread of electrical impulses in the cardiac muscle and the subsequent contraction-relaxation process are quantitatively described by the coupling of cardiac electro-mechanical models, which consists of the following four components, represented schematically in Fig. 1:

(1) the quasi-static finite elasticity model of the deformation of cardiac tissue, derived from a strain energy function which characterizes the anisotropic mechanical properties of the myocardium;
(2) the active tension model, consisting of a nonlinear ODE system, describing the intracellular calcium dynamics and the cross bridges binding, also called excitation–contraction coupling;
(3) the electrical current flow model of the cardiac tissue, i.e. the Bidomain model (or its reduction called Monodomain model), which is a degenerate parabolic system of two nonlinear partial differential equations (PDEs) of reaction–diffusion type, describing the evolution in space and time of the intra- and extracellular electric potentials;
(4) the membrane model of the cardiac myocyte, i.e. a stiff system of ordinary differential equations (ODEs), describing the flow of the ionic currents through the cellular membrane.

This complex nonlinear model poses great theoretical and numerical challenges.

At the theoretical level, the well-posedness of the cardiac electro-mechanical coupling model is still an open problem, as well as the convergence of its finite element approximation. The validity of the strong ellipticity condition has been
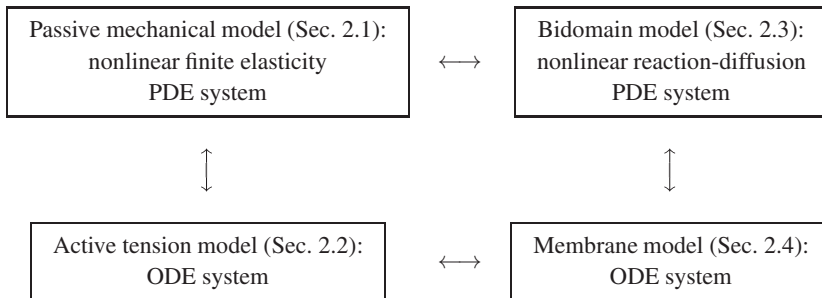

Fig. 1.   Schematic representation of the four main components of a cardiac electro-mechanical model.

investigated in Ref. 26 for the passive strain energy function and in Refs. 49 and 3 for the total energy, assuming that the active tension generated in a cardiac fiber is space independent. A partial result on the solvability of the coupled problem has been established recently in Ref. 4 for passive linear strain energy functions and for contraction models based on the active strain approach.

At the numerical level, the approximation and simulation of the cardiac electro-mechanical coupling model is a very demanding and expensive task, because of the very different space and time scales associated with the electrical and mechanical models, as well as their nonlinear and multiphysics interactions. Nevertheless, in recent years several research groups have developed electro-mechanical models assembling the main four components with different levels of coupling and description details.

In the quasi-static finite elasticity model, the most used strain energy function is the transversely isotropic exponential law by Guccione *et al.*[20] (see Refs. 1, 12, 14, 17, 22, 29, 36, 37 and 64). A few studies have considered orthotropic laws, see Refs. 7, 16, 18, 48 and 54, and isotropic laws, see Refs. 41 and 56.

Concerning the active tension development, phenomenological models have been considered in Refs. 7, 16, 18, 32, 36, 41, 54 and 56, while mechanistic models with a more detailed description of calcium dynamics and cross bridges binding have been used in Refs. 1, 14, 17, 22, 23, 29, 37, 48 and 64.

Regarding the electrical current flow model, the Bidomain model has been considered in Refs. 14, 16, 17, 22, 29 and 64, while most studies have employed reduced models such as the Monodomain model[1,7,18,32,36,37,41,48,54,56] or eikonal models.[33]

Regarding the ionic membrane model, phenomenological models have been used in Refs. 32, 36, 41, 54 and 56, while more detailed second generation membrane models related to different species have been considered in Refs. 1, 16, 17 and 37 (human), Refs. 23 and 64 (canine), Refs. 18 and 22 (rabbit), Refs. 14, 29 and 48 (guinea pig) and Ref. 7 (rat).

The coupling of Mono/Bidomain models with a mechanical model requires the Mono/Bidomain model to be posed on the deformed domain and this approach was adopted starting from the early works on electro-mechanical coupling, see Refs. 1, 2, 12, 16, 17, 19, 31, 32, 41, 46, 48, 49, 54, 65 34 and 43. Indeed, following the Lagrangian framework, in the reformulation of the Mono/Bidomain model on the reference domain the conductivity tensors appear to depend on the deformation gradient. This is traditionally called strong electro-mechanical coupling as opposed to the weak electro-mechanical coupling in which the Mono/Bidomain model is posed on the undeformed (or material) domain, see Refs. 34 and 43. We remark that in most of these studies the transformed conductivity tensor was correct only for isotropic media, while the correct form for more general anisotropic media appears in more recent works, see e.g. Refs. 2, 12, 19, 46, 49 and 54. Weak electro-mechanical coupling disregarding the effects of the deformation onto the electric current flow model has been considered especially in recent studies employing realistic cardiac geometries, for the practical reason to reduce the computational load of the

simulations by avoiding the reassembling of the stiffness matrices associated to the finite element approximation of the Monodomain[6,7,18,33,35,37,61] or Bidomain[14,22,64] model at each update of the domain deformation.

When a strong electro-mechanical coupling is adopted, i.e. the Monodomain or Bidomain model is posed on the deformed domain, the bioelectric activity experiences three main feedbacks from the mechanical deformation:

(i) conductivity feedback: the influence of the deformation gradient on the conductivity coefficients of the electric current flow model;
(ii) convection feedback: the influence of deformation gradient and deformation rate on the electric current flow model;
(iii) ionic feedback: the influence of stretch-activated membrane channels on the ionic current.

In Ref. 12, a strong electro-mechanical coupling was considered, i.e. the Bidomain model was solved on the deformed domain, but only with transversely isotropic anisotropy and a very simplified phenomenological active tension model; moreover the ionic and convective feedbacks were not taken into account or included in our model and simulations. Indeed, the presence of the convection feedback in the electric current flow model has never been taken into account in the literature. The effects of stretch-activated currents have been studied in Refs. 29 and 64 by solving the Bidomain model on the undeformed configuration, and in Refs. 1 and 32 by using the Monodomain model on the deformed configuration.

To our knowledge, the three main mechanical feedbacks (i), (ii) and (iii) have never been taken into account together, especially when the Bidomain model and orthotropic anisotropy properties are included in the electro-mechanical model. The goal of this work is to fill this gap by accurately deriving the mechanical feedbacks and by studying their effects in a strongly coupled anisotropic cardiac electro-mechanical model. To this end, we develop a strongly coupled electro-mechanical model by combining the following four components (presented in more details in Sec. 2): the orthotropic strain energy function from Ref. 18; the mechanistic active tension model proposed in Ref. 37; the orthotropic Bidomain model[11] in the deformed cardiac tissue; the ten Tusscher *et al.* membrane model[60] for human ventricular cells, augmented with stretch-activated channels. By means of 3D parallel numerical simulations, we evaluate quantitatively the effects of all mechanical feedbacks on the spatial distributions of activation and repolarization times, action potential duration, as well as on the morphology of electrograms. Our results show that mechanical feedbacks cannot be neglected, since the mechanical deformation affects the space–time evolution of the electrical potentials, mostly during the repolarization phase. Therefore, the modified Bidomain model that we have proposed and studied allows more accurate electro-mechanical simulations involving the repolarization phase.

The rest of the paper is organized as follows. In Sec. 2, we introduce the cardiac electro-mechanical model with its four main components; in Sec. 3, we describe the

numerical methods used for the solution of the electro-mechanical models; in Sec. 4, we present the results of the numerical simulations.

2. Cardiac Electro-mechanical Models

We now describe the four main components of the electro-mechanical model introduced in Fig. 1.

2.1. *Mechanical model of cardiac tissue*

Let us denote the material coordinates $\mathbf{X} = (X_1, X_2, X_3)^T$ of the undeformed or reference cardiac domain $\widehat{\Omega}$, the spatial coordinates $\mathbf{x} = (x_1, x_2, x_3)^T$ of the deformed cardiac domain at time t $\Omega(t)$. We denote by $\mathbf{x} = \Phi(\mathbf{X}, t) = \Phi_t(\mathbf{X})$ the deformation map between $\widehat{\Omega}$ and $\Omega(t) = \Phi_t(\widehat{\Omega})$ (see Fig. 2) and by $\mathbf{U}(\mathbf{X}, t) = \mathbf{x} - \mathbf{X} = \Phi(\mathbf{X}, t) - \mathbf{X}$ the displacement field.

We denote by Div and div (Grad and grad) the material and spatial divergence (gradient) of a vector (scalar), respectively. From a mechanical point of view, the cardiac tissue is modeled as a nonlinear elastic material. The deformation gradient tensor $\mathbf{F}$ and its determinant are given by

$$\mathbf{F}(\mathbf{X}, t) = \{F_{ij}\} = \left\{ \frac{\partial x_i}{\partial X_j}, \ i, j = 1, 2, 3 \right\}, \quad J(\mathbf{X}, t) = \det \mathbf{F}(\mathbf{X}, t).$$

The Cauchy–Green deformation tensor $\mathbf{C}$ and Green–Lagrange strain tensor $\mathbf{E}$ are

$$\mathbf{C} = \mathbf{F}^T \mathbf{F} \quad \text{and} \quad \mathbf{E} = \frac{1}{2}(\mathbf{C} - \mathbf{I}),$$

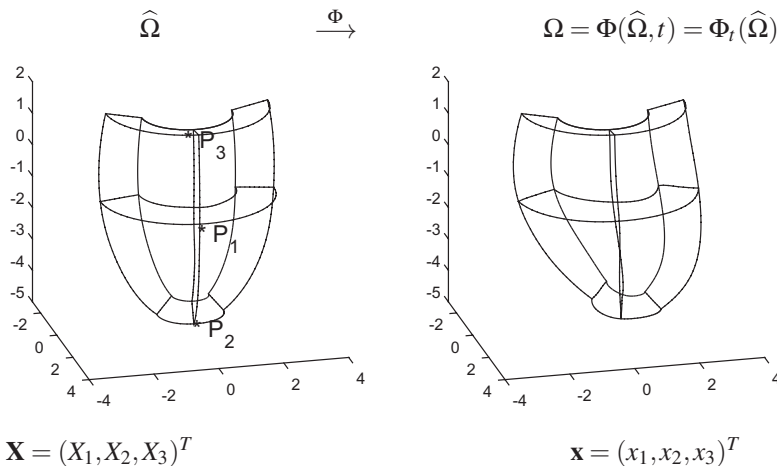where $\mathbf{I}$ denotes the identity matrix.

Fig. 2. Reference domain $\widehat{\Omega}$ with coordinates $\mathbf{X} = (X_1, X_2, X_3)^T$ (left) and deformed domain $\Omega = \Phi(\widehat{\Omega}, t) = \Phi_t(\widehat{\Omega})$ with coordinates $\mathbf{x} = (x_1, x_2, x_3)^T$ (right).

We first assume that the time-dependent inertial term in the governing elastic wave equation may be neglected, see e.g. Refs. 33 and 65. Thus, the steady-state force equilibrium equation reads

$$\mathrm{Div}(\mathbf{FS}(\mathbf{U}, \mathbf{X})) = \mathbf{0}, \quad \mathbf{X} \in \widehat{\Omega}, \tag{2.1}$$

where $\mathbf{S}$ is the second Piola–Kirchhoff stress tensor. We close the quasi-static mechanical model (2.1) by imposing a prescribed displacement on a Dirichlet boundary $\mathbf{x}(\mathbf{X}, t) = \widehat{\mathbf{x}}(\mathbf{X})$, $\mathbf{X} \in \partial\widehat{\Omega}_D$ and no traction force on a Neumann boundary $\mathbf{FS}(\mathbf{U}(\mathbf{X}, t), \mathbf{X})\,\mathbf{N} = \mathbf{0}$, $\mathbf{X} \in \partial\widehat{\Omega}_N$.

The tensor $\mathbf{S}$ is given by the sum of a passive elastic component $\mathbf{S}^{\mathrm{pas}}$, a volumetric component $\mathbf{S}^{\mathrm{vol}}$, and a biochemically generated active component $\mathbf{S}^{\mathrm{act}}$, i.e.

$$\mathbf{S} = \mathbf{S}^{\mathrm{pas}} + \mathbf{S}^{\mathrm{vol}} + \mathbf{S}^{\mathrm{act}},$$

as done in many previous studies, see e.g. Refs. 28, 33 and 63. An alternative approach, introduced in Ref. 8, consists of a multiplicative decomposition of the deformation gradient tensor $\mathbf{F}$ into a passive elastic deformation and an active stretch component, see also Refs. 2, 46 and 55.

The passive component $\mathbf{S}^{\mathrm{pas}}$ is computed from a suitable strain energy function W^{pas} and the Green–Lagrange strain $\mathbf{E}$ as

$$S_{ij}^{\mathrm{pas}} = \frac{1}{2}\left(\frac{\partial W^{\mathrm{pas}}}{\partial E_{ij}} + \frac{\partial W^{\mathrm{pas}}}{\partial E_{ji}}\right), \quad i, j = 1, 2, 3.$$

A wide variety of strain energy functions W^{pas} have been proposed and adopted in the literature, see e.g. Refs. 15, 19, 20, 26, 40, 53, 56, 58 and 62.

We recall that the cardiac tissue consists of an arrangement of fibers that rotate counterclockwise from epi- to endocardium, and that have a laminar organization modeled as a set of muscle sheets running radially from epi- to endocardium, e.g. Refs. 38 and 62. In the following, we will denote by $\widehat{\mathbf{a}}_l$, $\widehat{\mathbf{a}}_t$ and $\widehat{\mathbf{a}}_n$ the unit vectors of the local fiber coordinate system in the reference configuration. In particular, $\widehat{\mathbf{a}}_l$ represents the fiber direction and $\widehat{\mathbf{a}}_t$, $\widehat{\mathbf{a}}_n$ the two orthogonal cross fiber directions.

In this paper, the myocardium is modeled as an orthotropic hyperelastic material, with the exponential strain energy function

$$W^{\mathrm{pas}} = \frac{a}{2b}(e^{b(\mathbf{I}_1 - 3)} - 1) + \sum_{i=l,t}\frac{a_i}{2b_i}(e^{b_i(\mathbf{I}_{4i} - 1)^2} - 1) + \frac{a_{lt}}{2b_{lt}}(e^{b_{lt}\mathbf{I}_{8lt}^2} - 1), \tag{2.2}$$

see Ref. 18. Here $a, b, a_{(l,t,lt)}, b_{(l,t,lt)}$ are positive material parameters,

$$\mathbf{I}_1 = \mathrm{tr}(\mathbf{C}), \quad \mathbf{I}_{4l} = \widehat{\mathbf{a}}_l^T \mathbf{C}\widehat{\mathbf{a}}_l, \quad \mathbf{I}_{4t} = \widehat{\mathbf{a}}_t^T \mathbf{C}\widehat{\mathbf{a}}_t, \quad \mathbf{I}_{8lt} = \widehat{\mathbf{a}}_l^T \mathbf{C}\widehat{\mathbf{a}}_t.$$

The volumetric component $\mathbf{S}^{\mathrm{vol}}$ is given by

$$S_{ij}^{\mathrm{vol}} = \frac{1}{2}\left(\frac{\partial W^{\mathrm{vol}}}{\partial E_{ij}} + \frac{\partial W^{\mathrm{vol}}}{\partial E_{ji}}\right), \quad i, j = 1, 2, 3,$$

where W^{vol} is a volume change penalization term

$$W^{\mathrm{vol}} = K(J - 1)^2, \tag{2.3}$$

with K a positive bulk modulus, that is added to the strain energy function in order to model the myocardium as nearly incompressible.

The active component $\mathbf{S}^{\text{act}}$ is given by (2.5) below in terms of the active tension developed along the myofibers.

2.2. *Mechanical model of active tension*

The contraction of the ventricles results from the active tension generated by the model of myofilaments dynamics activated by calcium. We assume as in Refs. 48 and 65 that the generated active force acts only in the direction of the fiber, hence, according to Ref. 27, Chap. 10, the active Cauchy stress is

$$\sigma^{\text{act}}(\mathbf{x}, t) = J^{-1} T_a \mathbf{a}_l(\mathbf{x}) \otimes \mathbf{a}_l(\mathbf{x}),$$

where $\mathbf{a}_l = \dfrac{\mathbf{F}\widehat{\mathbf{a}}_l}{|\mathbf{F}\widehat{\mathbf{a}}_l|}$ is a unit vector parallel to the local fiber direction and T_a is the active fiber stress related to the deformed domain. In terms of the principal axes of the reference configuration, we obtain:

$$\mathbf{a}_l \otimes \mathbf{a}_l = \frac{\mathbf{F}\widehat{\mathbf{a}}_l \otimes \mathbf{F}\widehat{\mathbf{a}}_l}{\|\mathbf{F}\widehat{\mathbf{a}}_l\|^2} = \frac{\mathbf{F}\widehat{\mathbf{a}}_l \widehat{\mathbf{a}}_l^T \mathbf{F}^T}{\widehat{\mathbf{a}}_l^T \mathbf{C}\widehat{\mathbf{a}}_l}. \tag{2.4}$$

Then the second Piola–Kirchhoff active stress component is given by

$$\mathbf{S}^{\text{act}} = J\mathbf{F}^{-1}\sigma^{\text{act}}\mathbf{F}^{-T} = T_a \frac{\widehat{\mathbf{a}}_l \otimes \widehat{\mathbf{a}}_l}{\widehat{\mathbf{a}}_l^T \mathbf{C}\widehat{\mathbf{a}}_l}, \tag{2.5}$$

and the stretch along the fiber direction is given by

$$\lambda = \sqrt{\widehat{\mathbf{a}}_l^T \mathbf{C}\widehat{\mathbf{a}}_l}. \tag{2.6}$$

We remark that additional active components in the directions $\mathbf{a}_t, \mathbf{a}_n$ could also be considered. The biochemically generated active tension T_a is given by the model by Land *et al.*,[37] where the active tension $T_a = T_a(\text{Ca}_i, \lambda, \frac{d\lambda}{dt})$ is Calcium, stretch and stretch-rate dependent and its dynamics is described by the following system of ODEs:

$$\begin{cases} \dfrac{dtr}{dt} = k_{\text{tr}}\left(\left(\dfrac{\text{Ca}_i}{\text{Ca}_{50}(1 + \beta(\lambda - 1))}\right)^{n_{\text{tr}}}(1 - \text{tr}) - \text{tr}\right), \\[4mm] \dfrac{dxb}{dt} = k_{xb}\left(\text{tr}_{50}\text{tr}^{n_{xb}}(1 - xb) - \dfrac{1}{\text{tr}_{50}\text{tr}^{n_{xb}}}xb\right), \\[4mm] \dfrac{dQ_i}{dt} = A_i \dfrac{d\lambda}{dt} - \alpha_i Q_i, \quad i = 1, 2, \\[4mm] T_a = g(Q)h(\lambda)xb, \quad Q = Q_1 + Q_2, \end{cases} \tag{2.7}$$

with parameters $k_{\text{tr}}, k_{xb}, \text{Ca}_{50}, \text{tr}_{50} \in (0, 1), n_{\text{tr}}, n_{xb}, \beta > 1, A_1 < 0, A_2 > 0, \alpha_1, \alpha_2 > 0$, and non-decreasing, bounded, Lipschitz functions $h : \mathbb{R} \to \mathbb{R}$ and $g(Q) : \mathbb{R} \to \mathbb{R}$;

see Ref. 37 for more details. If we introduce the vector $\mathbf{z} = \{\text{tr}, \; xb, \; Q_1, \; Q_2\}$, then system (2.7) in compact form becomes

$$\begin{cases} \dfrac{d\mathbf{z}}{dt} = R_z\left(\mathbf{z}, \text{Ca}_i, \lambda, \dfrac{d\lambda}{dt}\right), \\[2mm] T_a = f_{T_a}(\mathbf{z}, \lambda). \end{cases} \tag{2.8}$$

Simplified stretch and stretch-rate independent models have also been considered, see e.g. Refs. 19 and 41.

2.3. *Electrical model of cardiac tissue: The Bidomain model on a deforming domain*

We recall that from a macroscopic point of view, the classical Mono/Bidomain model on a given domain is derived by imposing current conservation laws for the intra- and extracellular current assuming that the intra- and extracellular spaces are superimposed, occupy the same volume, are connected by a distributed membrane which is the active current source, and a quasi-static regime holds. This model has also been derived by homogenization of a network of cellular models (see Refs. 30, 42 and 51). In electro-mechanical models, the presence of the mechanical component entails that the bioelectrical component lives on the deformed cardiac domain. In this section, we proceed to derive a macroscopic Bidomain model using the same assumptions but considering a general moving domain.

Let $U \subset \widehat{\Omega}$ be an open connected subset of the undeformed domain. We assume that the deformation map $\Phi_t : \widehat{\Omega} \to \Omega(t)$ is sufficiently regular. We denote by $\rho_{i,e}$ the intra- and extracellular charge densities, by $u_{i,e}$ the intra- and extracellular electric potentials, by $\mathbf{J}_{i,e} = -D_{i,e}\nabla u_{i,e}$ the intra- and extracellular current densities, i.e. the total drift ionic current components, by i_m the transmembrane current per unit volume flowing from the intra- to the extracellular media, and by $\mathbf{n}$ the outward normal to $\Phi_t(U)$.

From the *charge conservation law*, we get the following master balance relationship (see e.g. Ref. 39) that holds for all $U \subset \widehat{\Omega}$:

$$\begin{cases} \dfrac{d}{dt}\displaystyle\int_{\Phi_t(U)} \rho_i d\mathbf{x} = -\int_{\partial\Phi_t(U)} \mathbf{J}_i \cdot \mathbf{n}d\sigma - \int_{\Phi_t(U)} i_m d\mathbf{x}, \\[4mm] \dfrac{d}{dt}\displaystyle\int_{\Phi_t(U)} \rho_e d\mathbf{x} = -\int_{\partial\Phi_t(U)} \mathbf{J}_e \cdot \mathbf{n}d\sigma + \int_{\Phi_t(U)} i_m d\mathbf{x}. \end{cases}$$

Then we define the deformation rate $\mathbf{V} = \frac{\partial\Phi_t}{\partial t}$ and by applying the Reynolds' *transport* theorem (see Ref. 25) and *divergence* theorems we obtain

$$\begin{cases} \dfrac{\partial\rho_i}{\partial t} + \text{div}(\rho_i\mathbf{V}) = -\text{div}\,\mathbf{J}_i - i_m, \quad \forall\,\mathbf{x} \in \Phi_t(\hat{\Omega}), \\[4mm] \dfrac{\partial\rho_e}{\partial t} + \text{div}(\rho_e\mathbf{V}) = -\text{div}\,\mathbf{J}_e + i_m, \quad \forall\,\mathbf{x} \in \Phi_t(\hat{\Omega}), \end{cases} \tag{2.9}$$

or equivalently

$$\begin{cases} \dfrac{\partial \rho_i}{\partial t} + \operatorname{div}(\rho_i \mathbf{V}) = -\operatorname{div} \mathbf{J}_i - i_m, & \forall\, \mathbf{x} \in \Phi_t(\hat{\Omega}) \\[2mm] \dfrac{\partial (\rho_i + \rho_e)}{\partial t} + \operatorname{div}((\rho_i + \rho_e)\mathbf{V}) = -\operatorname{div}(\mathbf{J}_i + \mathbf{J}_e), & \forall\, \mathbf{x} \in \Phi_t(\hat{\Omega}). \end{cases} \tag{2.10}$$

We observe that a system analogous to (2.10) has been derived in Ref. 13 by mixing macroscopic mass conservation laws and formal homogenization techniques, while our derivation is based on current conservation laws.

In system (2.10), new evolution and advection terms arise: the local rate of charge density change $\partial_t \rho_{i,e}$ which can be neglected by considering, as usual, quasi-static regimes, (see Refs. 21 and 52) and the advection term $\operatorname{div}(\rho_{i,e}\mathbf{V})$ associated with the charge transport due to the domain motion, where $\mathbf{V} = \frac{\partial \Phi_t}{\partial t}$ is the rate of deformation. In this derivation, it appears that the Bidomain model on a deformed domain considered in the works cited above, can be justified if the advection terms can be neglected. Indeed, since the charge densities are associated to concentrations of the main three Na^+, K^+, Ca^{2+}, i.e. $\rho_{i,e} = \sum_{s=1}^{s=3} F z_s c_s^{i,e}$, then $\operatorname{div}(\rho_{i,e}\mathbf{V}) = \rho_{i,e} \operatorname{div}(\mathbf{V}) + \nabla(\rho_{i,e}) \cdot \mathbf{V}$. Since the cardiac tissue can be considered almost-incompressible, i.e. $\operatorname{div}(\mathbf{V}) \approx 0$, then $\operatorname{div}(\rho_{i,e}\mathbf{V}) \approx \nabla(\rho_{i,e}) \cdot \mathbf{V} = \sum_{s=1}^{s=3} F z_s \nabla c_s^{i,e} \cdot \mathbf{V}$, which in turn can be neglected since the advection terms $\nabla c_s^{i,e} \cdot \mathbf{V}$ can be considered negligible in comparison with the total drift current $J_{i,e}$. Thus, the derived Bidomain model coincides with the classical Bidomain model but posed on a moving domain, i.e.

$$\begin{cases} \operatorname{div} \mathbf{J}_i + i_m = 0 & \text{in } \Omega(t), \\ \operatorname{div} \mathbf{J}_e - i_m = 0 & \text{in } \Omega(t), \end{cases} \tag{2.11}$$

or equivalently

$$\begin{cases} \operatorname{div} \mathbf{J}_i + i_m = 0 & \text{in } \Omega(t), \\ \operatorname{div}(\mathbf{J}_i + \mathbf{J}_e) = 0 & \text{in } \Omega(t). \end{cases} \tag{2.12}$$

We recall that the transmembrane current is the sum of a capacitative current and an ionic membrane current (see e.g. Ref. 11, Chap. 2):

$$i_m(\mathbf{x}, t) = c_m \frac{\partial v}{\partial t}(\mathbf{x}, t) + i_{\text{ion}}(v, \mathbf{w}, \mathbf{c}, \lambda), \quad \text{with}$$

- $v = u_i - u_e$ is the transmembrane potential,
- $\mathbf{w}$ are the gating variables,
- $\mathbf{c}$ are the ionic concentrations,
- λ is the stretch along the fiber direction (see (2.6)),

and $c_m = \chi C_m$, $i_{\text{ion}} = \chi I_{\text{ion}}$, where C_m is the membrane capacitance, I_{ion} the ionic membrane current (both for unit area of the membrane surface) and χ is the membrane surface to volume ratio. Here the gating variables $\mathbf{w}$ and ionic concentrations

c satisfy the ODE systems

$$\frac{\partial \mathbf{w}}{\partial t} - \mathbf{R}_w(v, \mathbf{w}) = 0, \quad \frac{\partial \mathbf{c}}{\partial t} - \mathbf{R}_c(v, \mathbf{w}, \mathbf{c}) = 0,$$

and the functions $I_{\mathrm{ion}}(v, \mathbf{w}, \mathbf{c})$, $R_w(v, \mathbf{w})$, $R_c(v, \mathbf{w}, \mathbf{c})$ are given by the chosen membrane model (defined below in Sec. 2.4). It follows that the full evolution system on the deformed medium $\Omega(t) = \Phi_t(\widehat{\Omega})$ is given by

$$\begin{cases} c_m \dfrac{\partial v}{\partial t} + i_{\mathrm{ion}}(v, \mathbf{w}, \mathbf{c}, \lambda) + \mathrm{div}\, \mathbf{J}_i = 0 & \text{in } \Omega(t), \\[2mm] \mathrm{div}(\mathbf{J}_e + \mathbf{J}_i) = 0 & \text{in } \Omega(t), \\[2mm] \dfrac{\partial \mathbf{w}}{\partial t} - \mathbf{R}_w(v, \mathbf{w}) = 0, \quad \dfrac{\partial \mathbf{c}}{\partial t} - \mathbf{R}_c(v, \mathbf{w}, \mathbf{c}) = 0 & \text{in } \Omega(t). \end{cases} \quad (2.13)$$

Assuming the tissue insulated, system (2.13) is closed by no-current and no-flux conditions at the boundary of the deformed medium, i.e.

$$\mathbf{n}^T \mathbf{J}_i = 0, \quad \mathbf{n}^T \mathbf{J}_e = 0 \quad \text{on} \quad \partial\Omega(t) = \Phi_t(\partial\widehat{\Omega}).$$

The initial conditions are imposed only on $v = u_i - u_e$, due to the degeneracy of the parabolic–elliptic system, and on the gating and ionic concentration variables:

$$v(\mathbf{x}, 0) = v_0(\mathbf{x}), \quad \mathbf{w}(\mathbf{x}, 0) = \mathbf{w}_0(\mathbf{x}), \quad \mathbf{c}(\mathbf{x}, 0) = \mathbf{c}_0(\mathbf{x}).$$

Considering an applied extracellular current per unit volume i_{app}^e, the Bidomain system on the deformed configuration can then be written in terms of the unknowns $v = u_i - u_e$, u_e and also using $\mathbf{J}_{i,e} = -D_{i,e}\nabla u_{i,e}$, thus obtaining the following equivalent formulation that will be considered from now on:

$$\begin{cases} c_m \dfrac{\partial v}{\partial t} + i_{\mathrm{ion}}(v, \mathbf{w}, \mathbf{c}, \lambda) - \mathrm{div}(D_i\nabla(v + u_e)) = 0 & \text{in } \Omega(t), \\[2mm] -\mathrm{div}(D_i\nabla v) - \mathrm{div}((D_i + D_e)\nabla u_e) = i_{\mathrm{app}}^e & \text{in } \Omega(t), \\[2mm] \dfrac{\partial \mathbf{w}}{\partial t} - \mathbf{R}_w(v, \mathbf{w}) = 0, \quad \dfrac{\partial \mathbf{c}}{\partial t} - \mathbf{R}_c(v, \mathbf{w}, \mathbf{c}) = 0 & \text{in } \Omega(t), \end{cases} \quad (2.14)$$

or its equivalent variational formulation on the deformed domain

$$\begin{cases} \displaystyle\int_{\Omega(t)} \left[c_m \frac{\partial v}{\partial t} + i_{\mathrm{ion}}(v, \mathbf{w}, \mathbf{c}, \lambda) \right] \psi d\mathbf{x} + \int_{\Omega(t)} (\nabla(v + u_e))^T D_i \nabla\psi d\mathbf{x} = 0, \\[3mm] \displaystyle\int_{\Omega(t)} (\nabla u_e)^T (D_i + D_e) \nabla\psi d\mathbf{x} = -\int_{\Omega(t)} (\nabla v)^T D_i \nabla\psi d\mathbf{x} + \int_{\Omega(t)} i_{\mathrm{app}}^e \psi d\mathbf{x}. \end{cases} \quad (2.15)$$

Modified Bidomain formulation on the reference domain. We now transform the parabolic–elliptic formulation of the Bidomain model in differential and variational form on the reference configuration, using the strong coupling framework, that will be used in the rest of the paper.

From a Lagrangian point of view, we denote by $\widehat{u}_{i,e}(\mathbf{X}, t)$, $\widehat{v}(\mathbf{X}, t) = \widehat{u}_i - \widehat{u}_e$, $\widehat{\mathbf{w}}(\mathbf{X}, t)$ and $\widehat{\mathbf{c}}(\mathbf{X}, t)$ the potentials, gating and ionic concentration variables on the reference domain $\widehat{\Omega}$.

Taking into account that

$$\frac{\partial \widehat{v}}{\partial t} = \frac{\partial v}{\partial t} + \nabla v \cdot \frac{\partial \Phi_t}{\partial t}, \quad \nabla v(\mathbf{x}, t) = \mathbf{F}^{-T} \operatorname{Grad} \widehat{v}(\mathbf{X}, t), \quad \text{and} \quad d\mathbf{x} = J d\mathbf{X},$$

then we obtain the following differential formulation on $\widehat{\Omega}$:

$$
\begin{cases}
c_m J \left(\dfrac{\partial \widehat{v}}{\partial t} - \mathbf{F}^{-T} \operatorname{Grad} \widehat{v} \cdot \mathbf{V} \right) \\
\quad - \operatorname{Div}(J \mathbf{F}^{-1} D_i \mathbf{F}^{-T} \operatorname{Grad}(\widehat{v} + \widehat{u}_e)) + J i_{\text{ion}}(\widehat{v}, \widehat{\mathbf{w}}, \widehat{\mathbf{c}}, \lambda) = 0, \\
-\operatorname{Div}(J \mathbf{F}^{-1} D_i \mathbf{F}^{-T} \operatorname{Grad} \widehat{v}) \\
\quad - \operatorname{Div}(J \mathbf{F}^{-1}(D_i + D_e) \mathbf{F}^{-T} \operatorname{Grad} \widehat{u}_e) = J \widehat{i}^e_{\text{app}}
\end{cases}
\tag{2.16}
$$

coupled with the ODE system in the variables $\mathbf{w}(\mathbf{x}, t), \mathbf{c}(\mathbf{x}, t)$ for all $\mathbf{x} \in \Omega(t)$ given by

$$\frac{\partial \mathbf{w}}{\partial t} - \mathbf{R}_w(v, \mathbf{w}) = 0, \quad \frac{\partial \mathbf{c}}{\partial t} - \mathbf{R}_c(v, \mathbf{w}, \mathbf{c}) = 0.$$

Here we have considered an applied extracellular current per unit volume $\widehat{i}^e_{\text{app}}$ and in order to close the Bidomain system we prescribe initial conditions

$$\widehat{v}(\mathbf{X}, 0) = \widehat{v}_0(\mathbf{X}) \quad \text{in } \widehat{\Omega}, \quad \mathbf{w}(\mathbf{x}, 0) = \mathbf{w}_0(\mathbf{x}), \quad \mathbf{c}(\mathbf{x}, 0) = \mathbf{c}_0(\mathbf{x}) \quad \text{in } \Omega(t),$$

and insulating boundary conditions on $\partial \widehat{\Omega} \times (0, T)$ (assuming the cardiac tissue Ω_t insulated) $\widehat{\mathbf{n}}^T \mathbf{F}^{-1} D_{i,e} \mathbf{F}^{-T} \operatorname{Grad} \widehat{u}_e = 0$ and $\widehat{\mathbf{n}}^T \mathbf{F}^{-1} D_i \mathbf{F}^{-T} \operatorname{Grad} \widehat{u}_i = 0 = \widehat{\mathbf{n}}^T \mathbf{F}^{-1} D_i \mathbf{F}^{-T} \operatorname{Grad}(\widehat{v} + \widehat{u}_e)$ (since $\widehat{u}_i = \widehat{v} + \widehat{u}_e$).

Using the previous boundary conditions, we obtain the equivalent variational formulation of the modified Bidomain system on the reference domain given by

$$
\begin{cases}
\displaystyle\int_{\widehat{\Omega}} J \left[c_m \left(\frac{\partial \widehat{v}}{\partial t} - \mathbf{F}^{-T} \operatorname{Grad} \widehat{v} \cdot \mathbf{V} \right) + i_{\text{ion}}(\widehat{v}, \widehat{\mathbf{w}}, \widehat{\mathbf{c}}, \lambda) \right] \psi d\mathbf{X} \\
\quad + \displaystyle\int_{\widehat{\Omega}} J (\operatorname{Grad}(\widehat{v} + \widehat{u}_e))^T \mathbf{F}^{-1} D_i \mathbf{F}^{-T} \operatorname{Grad} \psi d\mathbf{X} = 0, \\
\displaystyle\int_{\widehat{\Omega}} J (\operatorname{Grad} \widehat{u}_e)^T \mathbf{F}^{-1} (D_i + D_e) \mathbf{F}^{-T} \operatorname{Grad} \psi d\mathbf{X} \\
\quad = - \displaystyle\int_{\widehat{\Omega}} J (\operatorname{Grad} \widehat{v})^T \mathbf{F}^{-1} D_i \mathbf{F}^{-T} \operatorname{Grad} \psi d\mathbf{X} + \displaystyle\int_{\widehat{\Omega}} J \widehat{i}^e_{\text{app}} \psi d\mathbf{X},
\end{cases}
\tag{2.17}
$$

again coupled with the ODE membrane system.

In summary, the influence of the cardiac tissue deformation on the Bidomain model in the strong coupling framework is due to three different mechano-electrical

feedbacks:

(i) the presence of the deformation gradient $\mathbf{F}$ in the conductivity coefficients structure, i.e. $J\mathbf{F}^{-1}D_{i,e}\mathbf{F}^{-T}$;

(ii) the presence of the deformation gradient $\mathbf{F}$ and the deformation rate $\mathbf{V}$ in the convective term $\mathbf{F}^{-T}\operatorname{Grad}\widehat{v}\cdot\mathbf{V}$;

(iii) the presence of the stretch λ in the ionic membrane current $i_{\text{ion}}(\widehat{v},\widehat{\mathbf{w}},\widehat{\mathbf{c}},\lambda)$ due to the stretch-activated current.

Computation of the conductivity tensors $\widehat{D}_{i,e}(\mathbf{X})$ on the reference domain. We recall that the conductivity tensors are given on the deformed cardiac domain $\Omega(t)$ by

$$D_{i,e}(\mathbf{x}) = \sigma_l^{i,e}\mathbf{a}_l(\mathbf{x})\mathbf{a}_l^T(\mathbf{x}) + \sigma_t^{i,e}\mathbf{a}_t(\mathbf{x})\mathbf{a}_t^T(\mathbf{x}) + \sigma_n^{i,e}\mathbf{a}_n(\mathbf{x})\mathbf{a}_n^T(\mathbf{x}). \qquad (2.18)$$

Here $\mathbf{a}_l(\mathbf{x})$, $\mathbf{a}_t(\mathbf{x})$, $\mathbf{a}_n(\mathbf{x})$, is a triplet of orthonormal principal axes with $\mathbf{a}_l(\mathbf{x})$ parallel to the local fiber direction, $\mathbf{a}_t(\mathbf{x})$ and $\mathbf{a}_n(\mathbf{x})$ tangent and orthogonal to the radial laminae, respectively, and both being transversal to the fiber axis (see e.g. Ref. 38). Moreover, $\sigma_l^{i,e}$, $\sigma_t^{i,e}$, $\sigma_n^{i,e}$ are the conductivity coefficients in the intra- and extracellular media measured along the corresponding directions $\mathbf{a}_l$, $\mathbf{a}_t$, $\mathbf{a}_n$.

The computation of the tensors

$$\widehat{D}_{i,e}(\mathbf{X},t) = \mathbf{F}^{-1}(\mathbf{X},t)D_{i,e}(\mathbf{x}(\mathbf{X},t))\mathbf{F}^{-T}(\mathbf{X},t)$$

must be performed on the reference configuration $\widehat{\Omega}$. Using orthogonality of the principal axes the tensors can be written in the following two equivalent expressions:

$$D_{i,e} = \sigma_n\mathbf{I} + (\sigma_l^{i,e} - \sigma_n^{i,e})\mathbf{a}_l\otimes\mathbf{a}_l + (\sigma_t^{i,e} - \sigma_n^{i,e})\mathbf{a}_t\otimes\mathbf{a}_t, \qquad (2.19)$$

or

$$D_{i,e} = \sigma_t\mathbf{I} + (\sigma_l^{i,e} - \sigma_t^{i,e})\mathbf{a}_l\otimes\mathbf{a}_l + (\sigma_n^{i,e} - \sigma_t^{i,e})\mathbf{a}_n\otimes\mathbf{a}_n. \qquad (2.20)$$

Let us denote by $\widehat{\mathbf{a}}_l(\mathbf{X})$, $\widehat{\mathbf{a}}_t(\mathbf{X})$ the unit vectors parallel and across the local fiber direction in the tangent plane to the lamina in the reference configuration, respectively. Then, the unit vector parallel to the local fiber in the deformed configuration is given by

$$\mathbf{a}_l = \frac{\mathbf{F}\widehat{\mathbf{a}}_l}{\|\mathbf{F}\widehat{\mathbf{a}}_l\|} = \frac{\mathbf{F}\widehat{\mathbf{a}}_l}{\sqrt{\widehat{\mathbf{a}}_l^T\mathbf{C}\widehat{\mathbf{a}}_l}},$$

hence, in terms of the principal axes of the reference configuration, we have

$$\mathbf{a}_l\otimes\mathbf{a}_l = \frac{\mathbf{F}\widehat{\mathbf{a}}_l\widehat{\mathbf{a}}_l^T\mathbf{F}^T}{\widehat{\mathbf{a}}_l^T\mathbf{C}\widehat{\mathbf{a}}_l}.$$

Considering $\mathbf{F}\widehat{\mathbf{a}}_t$ the vector lies in the tangent plane of the deformed lamina, but it is not parallel to $\mathbf{a}_t$, since it is not orthogonal to $\mathbf{a}_l$. We consider the following orthogonal decomposition

$$\mathbf{F}\widehat{\mathbf{a}}_t = \alpha\mathbf{a}_l + \mathbf{s}_t, \quad \text{with} \quad \mathbf{s}_t^T\mathbf{a}_l = 0, \quad \text{and} \quad \alpha = \mathbf{a}_l^T\mathbf{F}\widehat{\mathbf{a}}_t = \frac{\widehat{\mathbf{a}}_l\mathbf{C}\widehat{\mathbf{a}}_t}{\sqrt{\widehat{\mathbf{a}}_l\mathbf{C}\widehat{\mathbf{a}}_l}}$$

hence it follows

$$\mathbf{b}_t = \mathbf{F}\widehat{\mathbf{b}}_t, \quad \text{with} \quad \widehat{\mathbf{b}}_t = \widehat{\mathbf{a}}_t - \frac{\widehat{\mathbf{a}}_l^T \mathbf{C} \widehat{\mathbf{a}}_t}{\widehat{\mathbf{a}}_l^T \mathbf{C} \widehat{\mathbf{a}}_l}, \quad \text{and} \quad \mathbf{a}_t = \frac{\mathbf{b}_t}{\|\mathbf{b}_t\|}.$$

Setting in terms of the principal axes of the reference configuration we obtain

$$\mathbf{a}_t \otimes \mathbf{a}_t = \frac{\mathbf{F}\widehat{\mathbf{b}}_t \otimes \mathbf{F}\widehat{\mathbf{b}}_t}{\|\mathbf{F}\widehat{\mathbf{b}}_t\|^2} = \frac{\mathbf{F}\widehat{\mathbf{b}}_t \widehat{\mathbf{b}}_t^T \mathbf{F}^T}{\widehat{\mathbf{b}}_t^T \mathbf{C} \widehat{\mathbf{b}}_t}.$$

Using the expression (2.19), the product $\widehat{D}_{i,e} = \mathbf{F}^{-1} D_{i,e} \mathbf{F}^{-T}$ can be written as

$$\widehat{D}_{i,e} = \sigma_n^{i,e} \mathbf{C}^{-1} + (\sigma_l^{i,e} - \sigma_n^{i,e}) \frac{\widehat{\mathbf{a}}_l \widehat{\mathbf{a}}_l^T}{\widehat{\mathbf{a}}_l^T \mathbf{C} \widehat{\mathbf{a}}_l} + (\sigma_t^{i,e} - \sigma_n^{i,e}) \frac{\widehat{\mathbf{b}}_t \widehat{\mathbf{b}}_t^T}{\widehat{\mathbf{b}}_t^T \mathbf{C} \widehat{\mathbf{b}}_t}.$$

In the reference configuration, the normal unit vector to the lamina surface is given by

$$\widehat{\mathbf{a}}_n = \widehat{\mathbf{a}}_l \wedge \widehat{\mathbf{a}}_t.$$

In the deformed configuration, the two vectors $\mathbf{F}\widehat{\mathbf{a}}_l$ and $\mathbf{F}\widehat{\mathbf{a}}_t$ are both tangent to the deformed lamina surface and the former gives the local fiber direction, but the latter is not a transversal fiber direction. Anyway, the unit normal $\mathbf{a}_n$ to the deformed surface lamina is given by

$$\mathbf{a}_n = \frac{\mathbf{F}\widehat{\mathbf{a}}_l \wedge \mathbf{F}\widehat{\mathbf{a}}_t}{|\mathbf{F}\widehat{\mathbf{a}}_l \wedge \mathbf{F}\widehat{\mathbf{a}}_t|}.$$

Since $\mathbf{A}\mathbf{u} \wedge \mathbf{A}\mathbf{v} = \det(\mathbf{A})\mathbf{A}^{-T}(\mathbf{u} \wedge \mathbf{v})$, we have $\mathbf{F}\widehat{\mathbf{a}}_l \wedge \mathbf{F}\widehat{\mathbf{a}}_t = J\mathbf{F}^{-T}(\widehat{\mathbf{a}}_l \wedge \widehat{\mathbf{a}}_t) = J\mathbf{F}^{-T}\widehat{\mathbf{a}}_n$, hence

$$\mathbf{a}_n = \frac{\mathbf{F}^{-T}\widehat{\mathbf{a}}_n}{|\mathbf{F}^{-T}\widehat{\mathbf{a}}_n|}, \quad \text{and} \quad \mathbf{a}_n \otimes \mathbf{a}_n = \frac{\mathbf{F}^{-T}\widehat{\mathbf{a}}_n \otimes \mathbf{F}^{-T}\widehat{\mathbf{a}}_n}{\widehat{\mathbf{a}}_n^T \mathbf{C}^{-1} \widehat{\mathbf{a}}_n}.$$

Finally, using the expression (2.20), the product $\widehat{D}_{i,e}(\mathbf{X}, t) = \mathbf{F}^{-1}(\mathbf{X}, t) D_{i,e} \times (\mathbf{x}(\mathbf{X}, t))\mathbf{F}^{-T}(\mathbf{X}, t)$ can be written as

$$\widehat{D}_{i,e}(\mathbf{X}, t) = \sigma_t^{i,e} \mathbf{C}^{-1}(\mathbf{X}, t) + (\sigma_l^{i,e} - \sigma_t^{i,e}) \frac{\widehat{\mathbf{a}}_l(\mathbf{X}) \otimes \widehat{\mathbf{a}}_l(\mathbf{X})}{\widehat{\mathbf{a}}_l^T(\mathbf{X}) \mathbf{C}(\mathbf{X}, t) \widehat{\mathbf{a}}_l(\mathbf{X})}$$

$$+ (\sigma_n^{i,e} - \sigma_t^{i,e}) \frac{\mathbf{C}^{-1}(\mathbf{X}, t)\widehat{\mathbf{a}}_n(\mathbf{X}) \otimes \mathbf{C}^{-1}(\mathbf{X}, t)\widehat{\mathbf{a}}_n(\mathbf{X})}{\widehat{\mathbf{a}}_n^T(\mathbf{X}) \mathbf{C}^{-1}(\mathbf{X}, t) \widehat{\mathbf{a}}_n(\mathbf{X})}, \quad (2.21)$$

where it is evident that the deformation time-dependent influence on the conductivity tensor $\widehat{D}_{i,e}(\mathbf{X}, t)$ arises from the presence of the terms $C(\mathbf{X}, t)$ and $C^{-1}(\mathbf{X}, t)$.

2.4. *Ionic membrane model and stretch-activated channel current*

The functions $I_{\text{ion}}(v, \mathbf{w}, \mathbf{c}, \lambda)$ ($i_{\text{ion}} = \chi I_{\text{ion}}$), $R_w(v, \mathbf{w})$ and $R_c(v, \mathbf{w}, \mathbf{c})$ in the Bidomain model (2.16) are given by the ionic membrane model by ten Tusscher *et al.*,[60] available from the cellML depository (models.cellml.org/cellml). This model consists of 17 ordinary differential equations modeling the dynamics of the main ionic

currents $(I_{Na}, I_{to}, I_{Kr}, I_{Ks}, I_{K1}, I_{CaL})$ through the membrane of human ventricular myocytes. Other biophysically detailed ionic models could be used as well, see e.g. Ref. 11, Chap. 2.9. The ionic current is the sum $I_{ion}(v, \mathbf{w}, \mathbf{c}, \lambda) = I_{ion}^m(v, \mathbf{w}, \mathbf{c}) + I_{SAC}$ of the ionic term $I_{ion}^m(v, \mathbf{w}, \mathbf{c})$ given by the 10 Tusscher model and a stretch-activated channel current I_{SAC}. This last current is modeled as in Ref. 44 as the sum of non-specific and specific currents $I_{SAC} = I_{SAC,n} + I_{Ko}$. The non-specific current is defined by $I_{SAC,n} = I_{SAC,Na} + I_{SAC,K}$, with

$$I_{SAC,Na} = g_{SAC}\gamma_{SLSAC}(v - E_{Na})\left(-\frac{E_R + 85}{E_R - 65}\right),$$

$$I_{SAC,K} = g_{SAC}\gamma_{SLSAC}(v - E_K),$$

where $g_{SAC} = 4.13 \cdot 10^{-3}$, $\gamma_{SLSAC} = 10(\lambda - 1)$, $E_R = -10$. The specific stretch-dependent K^+ current is defined by

$$I_{Ko} = g_{Ko}\frac{\gamma_{SL,Ko}}{1 + \exp(-(10 + v)/45)}(v - E_K), \quad \text{where} \quad \gamma_{SL,Ko} = 3(\lambda - 1) + 0.7.$$

For related models of stretch-activated currents, we refer e.g. to Refs. 1, 29, 31 and 59.

3. Numerical Methods

The intrinsic multiscale structure of the cardiac electro-mechanical coupling allows us to adopt different space and time discretization parameters for the electrical and mechanical submodels. Indeed, the propagation of the electrical impulse in the myocardium is characterized by a sharp moving layer, the activation wavefront, with a depth of about 1 mm, which requires a spatial mesh size of 0.1 mm to be accurately catched by solving the Bidomain model. Moreover, the upstroke time constant of the transmembrane action potential is about 1.5–2 ms, hence the electrical time step size to solve the Bidomain equations should be on the order of hundredths of ms. On the other hand, the mechanical contraction and relaxation of the cardiac muscle do not present moving layers, therefore a larger spatial mesh size on the order of mm can be used to solve the finite elasticity system. Furthermore, the active tension generation does not exhibit a fast dynamics, allowing a larger mechanical time step size on the order of tenth of ms. Thus, the use of different time step and meshes sizes for the electric and mechanical components requires interpolation and synchronization among different meshes.

3.1. *Space discretization*

We discretize the cardiac domain with an hexahedral structured grid $\mathscr{T}_{h_m}$ for the mechanical model (2.1) and $\mathscr{T}_{h_e}$ for the electrical Bidomain model (2.16), where $\mathscr{T}_{h_e}$ is a refinement of $\mathscr{T}_{h_m}$, i.e. h_m is an integer multiple of h_e. We then discretize all scalar and vector fields of both mechanical and electrical models by isoparametric Q_1 finite elements in space.

3.2. *Time discretization*

The time discretization is performed by a semi-implicit splitting method. For simplicity, we describe the procedure in the case of equal mechanical and electrical time steps, but the two time steps can be chosen independently (as we mentioned before, the electrical time step is typically smaller). From now on, for simplicity of notations, we will drop the $\widehat{}$ notation for the functions and objects defined on the reference configuration. At each time step:

(a) given v^n, w^n, c^n at time t_n, solve the ODE system of the membrane model (Sec. 2.4) with a first-order implicit-explicit (IMEX) method to compute the new w^{n+1}, c^{n+1}:

$$
\begin{aligned}
w^{n+1} &= w^n + \Delta t_n R_w(v^n, w^{n+1}), \\
c^{n+1} &= c^n + \Delta t_n R_c(v^n, w^{n+1}, c^n);
\end{aligned}
\tag{3.1}
$$

(b) given the calcium concentration Ca_i^{n+1}, which is included in the concentration variables c^{n+1}, solve the mechanical problems (2.1) and (2.8) to compute the new deformed coordinates $\mathbf{x}^{n+1}$, providing the new deformation gradient tensor $\mathbf{F}_{n+1}$:

$$
\begin{aligned}
\mathbf{z}^{n+1} &= \mathbf{z}^n + \Delta t R_z\left(\mathbf{z}^{n+1}, \mathrm{Ca}_i^{n+1}, \lambda^{n+1}, \frac{\lambda^{n+1} - \lambda^n}{\Delta t_n}\right), \\
T_a^{n+1} &= f_{Ta}(\mathbf{z}^{n+1}, \lambda^{n+1}),
\end{aligned}
\tag{3.2}
$$

$$
\mathrm{Div}(\mathbf{F}_{n+1}\mathbf{S}_{n+1}) = 0,
$$

with

$$
\mathbf{S}_{n+1} = \mathbf{S}^{\mathrm{pas}}(\mathbf{C}_{n+1}) + \mathbf{S}^{\mathrm{vol}}(\mathbf{C}_{n+1}) + \mathbf{S}^{\mathrm{act}}(\mathbf{C}_{n+1}, T_a^{n+1});
$$

(c) given w^{n+1}, c^{n+1}, $\mathbf{F}_{n+1}$ and $J_{n+1} = \det(\mathbf{F}_{n+1})$, $\widehat{D}_{i,e}^{n+1} = \widehat{D}_{i,e}(\mathbf{X}, t_{n+1})$ solve the Bidomain system (2.16) with a first-order IMEX method and compute the new electric potentials v^{n+1}, u_e^{n+1} with the following operator splitting method:

(c1) compute u_e^{n+1} by solving the elliptic equation in (2.16):

$$
\begin{aligned}
&-\mathrm{Div}(J_{n+1}(\widehat{D}_i^{n+1} + \widehat{D}_e^{n+1})\,\mathrm{Grad}\,u_e^{n+1}) \\
&= -\mathrm{Div}(J_{n+1}\widehat{D}_i^{n+1}\,\mathrm{Grad}\,v^n) + i_{\mathrm{app}}^{e,n+1};
\end{aligned}
\tag{3.3}
$$

(c2) compute v^{n+1} by solving the parabolic equation in (2.16):

$$
\begin{aligned}
&c_m J_{n+1} \frac{v^{n+1}}{\Delta t_2} - \mathrm{Div}(J_{n+1}\widehat{D}_i^{n+1}\,\mathrm{Grad}(v^{n+1})) \\
&= c_m J_{n+1}\left(\frac{v^n}{\Delta t_n} + \mathbf{F}_{n+1}^{-T}\,\mathrm{Grad}(v^n)\frac{\mathbf{x}^{n+1} - \mathbf{x}^n}{\Delta t_n}\right) \\
&\quad + \mathrm{Div}(J_{n+1}\widehat{D}_i^{n+1}\,\mathrm{Grad}(u_e^{n+1})) \\
&\quad - J_{n+1}i_{\mathrm{ion}}(v^n, w^{n+1}, c^{n+1}, \lambda^{n+1}).
\end{aligned}
\tag{3.4}
$$

We remark that the finite elasticity equation should be solved coupled with the active tension model, in order to ensure convergence of the Newton method, as already described in Refs. 45 and 49. Moreover, we observe that the smoother dynamics of the myofiber active tension permits to use a mechanical time step larger than the electrical time step. In such a case, the stiffness matrices and right-hand sides in (3.3) and (3.4) need to be reassembled not at every electrical time step but only when the mechanical time step is updated. Note finally that, to approximate in the variational formulation the convective term in the right-hand side of (3.4), an *upwind* computation of the nodal gradient of v^n, based on the local orthonormal coordinate system associated to the ellipsoidal coordinates, is derived, projected onto the deformation rate $\frac{\mathbf{x}^{n+1} - \mathbf{x}^n}{\Delta t_n}$ vector and then integrated against the test function, see e.g. Ref. 47. We refer to Ref. 10 for more details, other variants of operator splitting and a comparison between coupled and uncoupled operator splitting techniques for the Bidomain system.

3.3. *Computational kernels*

Due to the employed space and time discretization strategies, at each time step, the main computational efforts consist of

(a) solving the nonlinear system deriving from the discretization of the mechanical problem (3.2). To this end, we use the Newton method with a GMRES iterative solver for the linear Jacobian system at each Newton step

$$Kw = f, \tag{3.5}$$

preconditioned by the Algebraic Multigrid preconditioner BoomerAMG,[24] provided within the Hypre library;

(b) solving the two linear systems (3.3) and (3.4) associated with the elliptic and parabolic equations deriving from the Bidomain model operator splitting procedure. For both systems, we use the Conjugate Gradient method preconditioned by a Multilevel Additive Schwarz preconditioner studied in Refs. 50 and 57; inexact ILU(0) solvers are used for the local problems on the subdomains.

Both mechanical and Bidomain solvers, together with the ODE solvers for the ionic and active tension models, are parallelized in space using a domain decomposition approach based on the parallel library PETSc.[5] This parallel library developed at the Argonne National Laboratory provides a suite of data structures and functions for building large-scale parallel scientific applications, based on the MPI communication library. The parallel strategy employed assigns each subdomain to one processor and the information associated with the interior of the subdomain is uniquely owned by that processor. The processor stores all subvectors and a block of the matrices (mass, stiffness) associated to each overlapping subdomain.

4. Simulation Results

In this section, we present the results of parallel numerical experiments performed on the BlueGene/Q Cluster (www.cineca.it/en/content/fermi-bgq) of the Cineca Consortium (www.cineca.it) and on the Linux cluster of the Department of Mathematics of the University of Milan (cluster.mat.unimi.it/). Our FORTRAN-90 code is based on the parallel library PETSc,[5] from the Argonne National Laboratory.

Domain geometry and fiber structure. The domain $\widehat{\Omega} = \Omega(0)$ is the image of a cartesian slab using ellipsoidal coordinates, yielding a portion of truncated ellipsoid. The family of truncated ellipsoids is described by the parametric equations

$$\begin{cases} x = a(r)\cos\theta\cos\phi, & \phi_{\min} \leq \phi \leq \phi_{\max}, \\ y = b(r)\cos\theta\sin\phi, & \theta_{\min} \leq \theta \leq \theta_{\max}, \\ z = c(r)\sin\theta, & 0 \leq r \leq 1, \end{cases} \tag{4.1}$$

where $a(r) = a_1 + r(a_2 - a_1)$, $b(r) = b_1 + r(b_2 - b_1)$, $c(r) = c_1 + r(c_2 - c_1)$, and $a_i, b_i, c_i, i = 1, 2$, are given coefficients determining the main axes of the ellipsoid. The fibers rotate intramurally linearly with the depth for a total amount of $120°$ proceeding counterclockwise from epicardium to endocardium. More precisely, in a local ellipsoidal reference system $(\mathbf{e}_\phi, \mathbf{e}_\theta, \mathbf{e}_r)$, the fiber direction $\mathbf{a}_l(\mathbf{x})$ at a point $\mathbf{x}$ is given by

$$\mathbf{a}_l(\mathbf{x}) = \mathbf{e}_\phi\cos\alpha(r) + \mathbf{e}_\theta\sin\alpha(r), \quad \text{with} \quad \alpha(r) = \frac{2}{3}\pi(1-r) - \frac{\pi}{4}, \quad 0 \leq r \leq 1.$$

Conductivity coefficients and strain energy function parameters. The values of the orthotropic conductivity coefficients (see (2.18)) used in all the numerical tests are the following:

$$\sigma_l^i = 3, \quad \sigma_t^i = 0.31525, \quad \sigma_n^i = 0.031525,$$
$$\sigma_l^e = 2, \quad \sigma_t^e = 1.3514, \quad \sigma_n^i = 0.6757,$$

where all values are expressed in $m\Omega^{-1}cm^{-1}$. This choice of parameters yields physiological propagation velocities of the excitation wavefront along and across fiber of about of 0.05, 0.03, 0.015 cm ms^{-1}, see e.g. Ref. 9. In the orthotropic strain energy function (2.2), the values of the parameters are chosen as in the original work,[18] i.e.

$$a = 0.333\,\text{kPa}, \quad a_l = 18.535\,\text{kPa}, \quad a_t = 2.564\,\text{kPa}, \quad a_{lt} = 0.417\,\text{kPa}$$
$$b = 9.242, \quad b_l = 15.972, \quad b_t = 10.446, \quad b_{lt} = 11.602.$$

The bulk modulus is $K = 200\,\text{kPa}$.

Stimulation site, initial and boundary conditions. The depolarization process is started by applying a cathodal extracellular stimulus of $i_{\text{app}}^e = -200\,\text{mA/cm}^3$ lasting 1 ms on a small volume of $0.4 \times 0.4 \times 0.2\,\text{mm}^3$ located in the center of the endocardial surface. The initial conditions are at resting values for all the potentials

and gating variables of the ten Tusscher model, while the boundary conditions are
for insulated tissue. In all the electro-mechanical simulations, the electrical mesh
size is $h_e = 0.01$ cm, while the mechanical mesh size is $h_m = 0.08$ cm (except
otherwise stated), and the electrical time step size is $\Delta_e t = 0.05$ ms, while the
mechanical times step is $\Delta_m t = 0.25$ ms.

Computation of activation and repolarization time. For each computational
node $\mathbf{x}$, the activation time (AT) is defined as the unique instant $t_a(\mathbf{x})$ during the
upstroke phase of the action potential when $v(\mathbf{x}, t_a(\mathbf{x})) = -50$ mV. The repolar-
ization time (RT) is defined as the unique instant $t_r(\mathbf{x})$ during the repolarization
phase of the action potential when $v(\mathbf{x}, t_r(\mathbf{x})) = 0.9 v_r$, with v_r resting potential.
The action potential duration (APD) is the difference $\mathrm{APD}(\mathbf{x}) = t_r(\mathbf{x}) - t_a(\mathbf{x})$.

Cellular membrane properties. We have considered homogeneous properties
of the cellular membrane, with a constant intrinsic APD of about 260 ms. We
have considered this simple setting in order to detect the effective influence of the
mechanical feedbacks, that otherwise could be masked by transmural and apico-
basal heterogeneities of the cellular membrane.

4.1. *Parallel scalability test*

In order to validate the effectiveness of our electro-mechanical solver, we first con-
sider a weak scaling test on truncated ellipsoidal domains of increasing size, mod-
eling portions of the ventricular wall. The results for the mechanical solver are
reported in Table 1. The number of subdomains (and processors) is increased from
64 to 1024, with the largest domain being an half ellipsoid with parameters in (4.1)
given by $a_1 = b_1 = 1.5$, $c_1 = 4.4$, $a_2 = b_2 = 2.7$, $c_2 = 5$, all in cm, and $\phi_{\min} = -\pi/2$,
$\phi_{\max} = \pi/2$, $\theta_{\min} = -3\pi/8$, $\theta_{\max} = \pi/8$. The physical dimensions of the increasing
ellipsoidal domains are chosen so that the electrical mesh size h is kept fixed to
the value of about $h = 0.01$ cm, so as to keep the local mesh on each subdomain
fixed at $32 \cdot 32 \cdot 32$. The mechanical mesh size is four times the electrical one, thus

Table 1.   Weak scaling test, mechanical solver with AMG precon-
ditioner.

procs	dof	nit	lit	$time_{as}$	$time_{gmres}$	$time_{newton}$
64	109 395	2	75	3.52	7.06	19.84
128	215 475	2	74	3.52	8.13	21.84
256	427 635	2	79	3.52	9.20	23.88
512	848 691	2	80	3.52	15.21	43.52
1024	1 690 803	2	79	3.52	23.79	63.44

Number of processors (procs), degrees of freedom (dof), Newton iter-
ations (nit), GMRES iteration counts (lit) per Newton iteration,
CPU time in seconds for Jacobian assembling ($time_{as}$), for solv-
ing one Jacobian system ($time_{gmres}$), for the total Newton solve
($time_{newton}$).

on each subdomain the local mechanical mesh is $8 \cdot 8 \cdot 8$. With these choices, the global size of the discrete Bidomain system increases from about 4 millions degrees of freedom (dof) for the smallest domain with 64 subdomains to 68 millions dof for the largest domain with 1024 subdomains, and the discrete nonlinear elasticity system increases from about 100 thousands to 1.7 million dof. The simulation is run for 10 time steps of 0.05 ms during the excitation phase and the reported quantities are the results at the 10th time step.

The results reported in Table 1 show that both the nonlinear Newton iteration (nit) and linear GMRES iteration (lit) are completely scalable. The scalability of the GMRES iterations is achieved by the use of the AMG preconditioner. Nevertheless, the CPU times are not scalable, because they increase with the number of
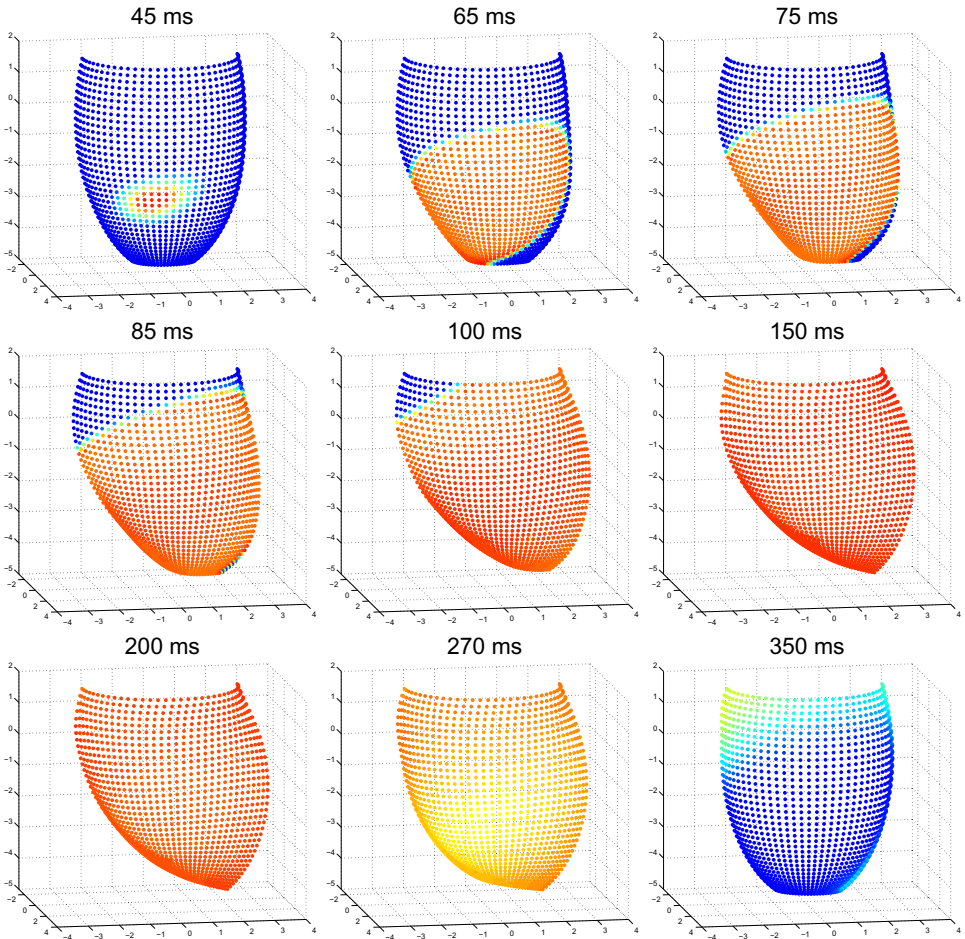

Fig. 3.   (Color online) Mechanical deformation of the cardiac domain at selected time instants (for the test). The colors denote the value of the transmembrane potential v at each point, ranging from resting (blue) to excited (red) values.

processors, due to the setup and cost of the AMG preconditioner at each Newton iteration.

4.2. *Effects of mechanical feedbacks*

We have performed four simulations of a whole cardiac heart beat:

- one disregarding the mechanical feedbacks (MF) in the Bidomain model (denoted by "without MF");
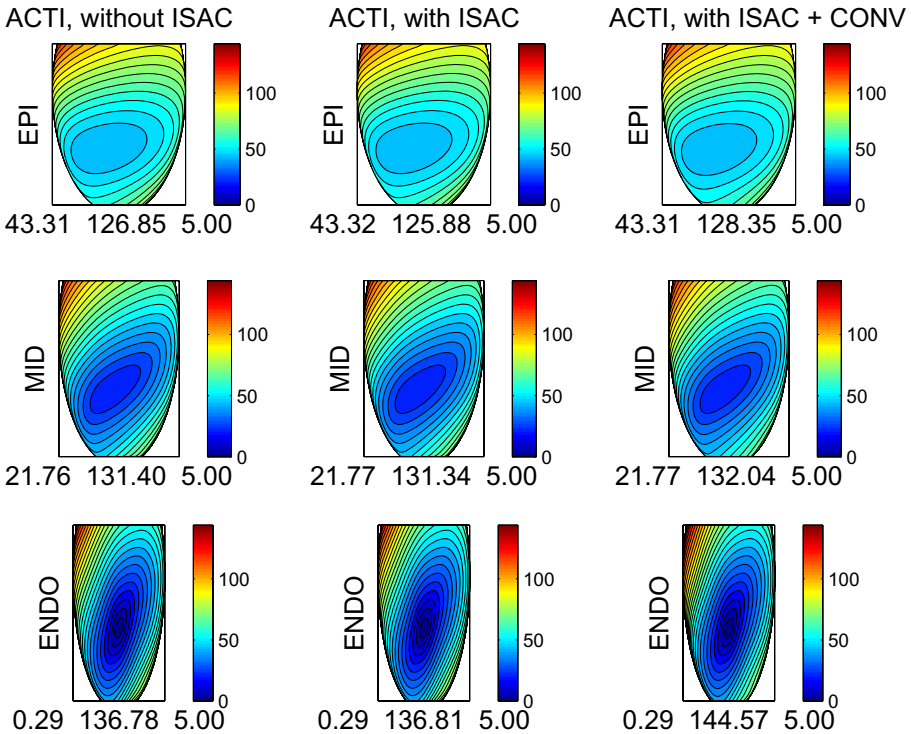

Fig. 4.   Activation (ACTI) time distributions on the endocardial, midmyocardial and epicardial surfaces computed without I_{SAC} current, with I_{SAC} current and with $I_{SAC} + CONV$ term. Below each panel are reported the min, max and step in ms of the displayed map.

Table 2.   Dispersion (difference between maximum and minimum value) in ms of activation time (AT), repolarization time (RT) and action potential duration (APD) without MF (first column) and in the three cases with MF: without I_{SAC} (second column), with I_{SAC} (third column), with $I_{SAC} + CONV$ (fourth column).

	without MF	without I_{SAC}	with I_{SAC}	with $I_{SAC} + CONV$
AT dispersion	141	138	138	144
RT dispersion	139	136	132	129
APD dispersion	13	14	27	45

- one taking into account the MF in the diffusion tensors of the Bidomain model, but disregarding the I_{SAC} current and the convective term (denoted by "without I_{SAC}");
- one taking into account the MF in the diffusion tensors and the I_{SAC} current, but disregarding the convective term (denoted by "with I_{SAC}");

Table 3.   Relative discrepancies of activation time (AT, first row), repolarization time (RT, second row) and action potential duration (APD, third row) distributions, transmembrane potential v at 100 ms (fourth row), extracellular potential u_e at selected points (fifth row) with respect to the associated reference quantity computed without MF.

	$\star = \mathrm{MF}$ without I_{SAC}	$\star = \mathrm{MF}$ with I_{SAC}	$\star = \mathrm{MF}$ with $I_{SAC} + \mathrm{CONV}$
$\|\mathrm{AT}_\star - \mathrm{AT}_{\mathrm{ref}}\|_\infty / \|\mathrm{AT}_{\mathrm{ref}}\|_\infty$	3e$-$2	3e$-$2	1e$-$1
$\|\mathrm{RT}_\star - \mathrm{RT}_{\mathrm{ref}}\|_\infty / \|\mathrm{RT}_{\mathrm{ref}}\|_\infty$	8e$-$3	4e$-$2	7e$-$2
$\|\mathrm{APD}_\star - \mathrm{APD}_{\mathrm{ref}}\|_\infty / \|\mathrm{APD}_{\mathrm{ref}}\|_\infty$	1e$-$2	6e$-$2	1e$-$1
$\|v(\cdot,100)_\star - v(\cdot,100)_{\mathrm{ref}}\|_1 / \|v(\cdot,100)_{\mathrm{ref}}\|_1$	1e$-$2	1.3e$-$1	1.6e$-$1
$\frac{1}{24}\sum_{i=1}^{24}\|u_e(\mathbf{x}_i,\cdot)_\star - u_e(\mathbf{x}_i,\cdot)_{\mathrm{ref}}\|_1$	3e$-$2	2.7e$-$1	3.4e$-$1

The symbol $\star$ denotes one of the three cases with MF: without I_{SAC} (first column), with I_{SAC} (second column) and with $I_{SAC} + \mathrm{CONV}$ (third column).
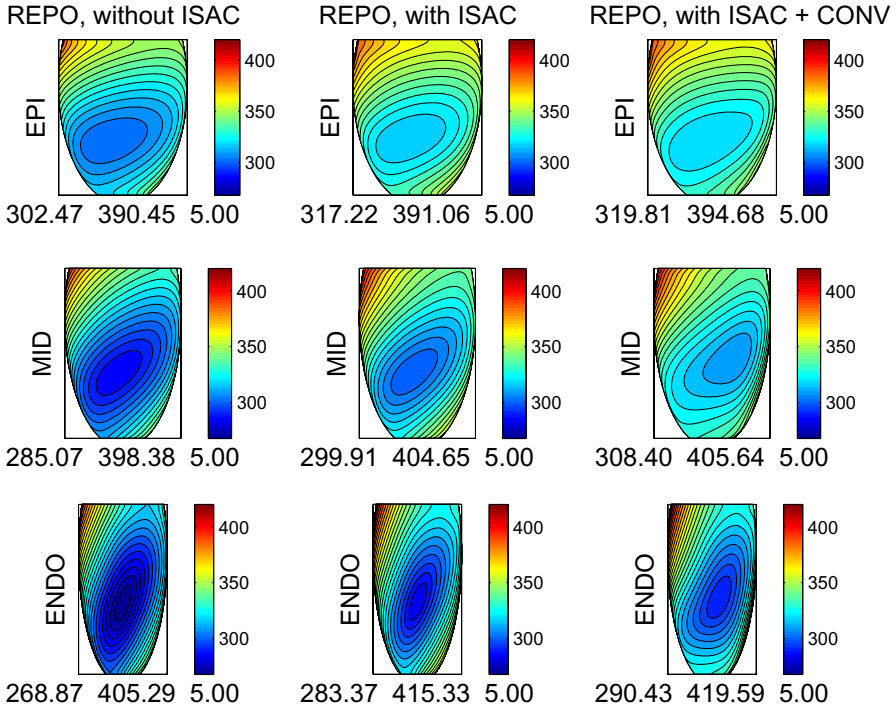

Fig. 5.   Repolarization (REPO) time distributions on the endocardial, midmyocardial and epicardial surfaces computed without I_{SAC} current, with I_{SAC} current and with $I_{SAC} + \mathrm{CONV}$ term. Below each panel are reported the min, max and step in ms of the displayed map.

- one taking into the MF the diffusion tensors, the I_{SAC} current and the convective term (denoted by "with I_{SAC} + CONV").

We report in Fig. 3 the transmembrane potential distributions on the deforming epicardial surface at nine selected time instants, ranging from 45 ms (at the beginning of activation) to 350 ms (at the end of repolarization).

Effects of mechanical feedbacks on the activation time. Figure 4 reports the activation time (AT) distributions on the endocardial, midmyocardial and epicardial surfaces relative to the three simulations with MF: without I_{SAC}, with I_{SAC} and with I_{SAC} + CONV. The AT distributions relative to the simulation without MF are not shown, because the visual inspection does not show any particular difference compared to the case without I_{SAC}. The total AT dispersions are reported in the first line of Table 2. The AT patterns in all the four cases present the same features, with the activation wavefront starting from the stimulus electrode applied at the center of the endocardium, then moving with an ellipsoidal shape fast along the fiber direction and slow across. The convective term slows down the propagation velocity across fiber, producing an AT delay of about 4–5 ms, see Table 3 for the relative error.
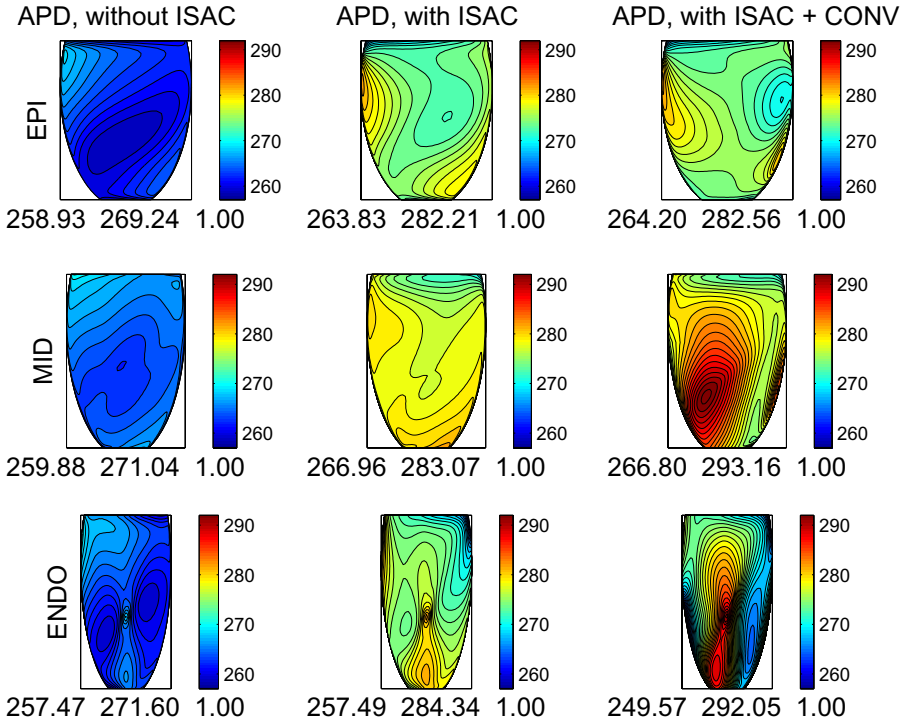

Fig. 6.   Action potential duration (APD) distributions on the endocardial, midmyocardial and epicardial surfaces computed without I_{SAC} current, with I_{SAC} current and with I_{SAC} + CONV term. Below each panels are reported the min, max and step in ms of the displayed map.

Effects of mechanical feedbacks on the repolarization time. Figure 5 reports the repolarization time (RT) distributions on the endocardial, midmyocardial and epicardial surfaces relative to the three simulations with MF: without I_{SAC}, with I_{SAC} and with $I_{SAC} + CONV$. The total RT dispersions are reported in the second line of Table 2. As for the AT, the RT distributions relative to the simulation without MF are not shown, because they are almost equal to the case without I_{SAC}. The presence of the I_{SAC} current produces an RT increase of about 10–15 ms and reduces the total RT dispersion of about 5 ms. The effect of the convective term on the RT is a further prolongation of 3–5 ms, and a further reduction of the RT dispersion of about 3 ms.
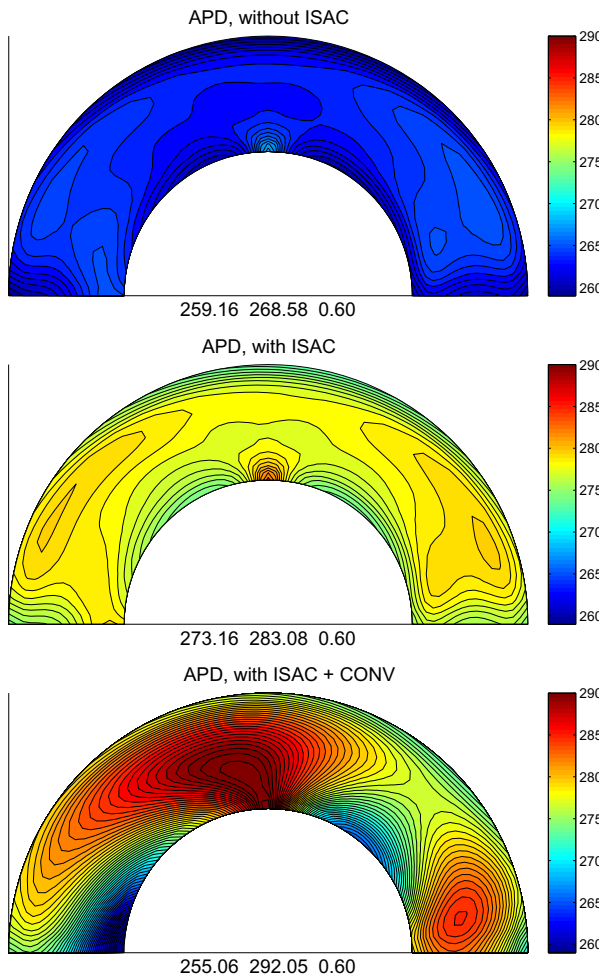

Fig. 7. Horizontal transmural action potential duration (APD) distributions, without I_{SAC} current (left), with I_{SAC} current (center) and with $I_{SAC} + CONV$ term (right). Below each panel are reported the min, max and step in ms of the displayed map.

Effects of mechanical feedbacks on the action potential duration. Figure 6 reports the action potential duration (APD) distributions on the endocardial, mid-myocardial and epicardial surfaces relative to the three simulations with MF: without I_{SAC}, with I_{SAC} and with $I_{\mathrm{SAC}}+$CONV. The total APD dispersions are reported in the third line of Table 2. The presence of the I_{SAC} current prolongs the APD of about 10–15 ms and strongly increases the total APD dispersion with respect to the simulation without I_{SAC} (from 27 to 14 ms). The convective term increases further the APD dispersion to 45 ms. We note that, in the case with $I_{\mathrm{SAC}}+$CONV, the total APD dispersion of 45 ms almost coincides with the endocardial dispersion, while the epicardial dispersion is comparable with that of the case with I_{SAC} and without the convective term (Table 2).

Figures 7 and 8 report the APD distributions on a central horizontal and a central vertical transmural sections of the truncated ellipsoid, respectively. The transmural APD dispersions in the cases without I_{SAC} and with I_{SAC} are comparable and small, in the range 10–13 ms. Instead, in the simulation with $I_{\mathrm{SAC}}+$CONV, the APD transmural dispersion increases significantly, being 37 ms in the horizontal section and 22 ms in the vertical section. Thus, the convective term seems to induce transmural and circumferential APD heterogeneities.
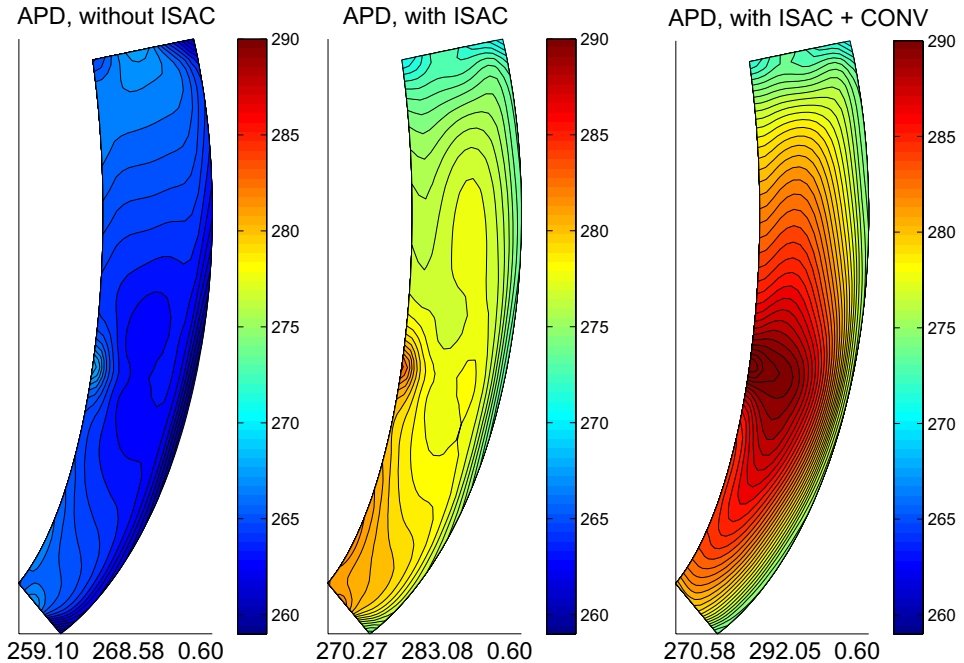

Fig. 8.   Vertical transmural action potential duration (APD) distributions, without I_{SAC} current (left), with I_{SAC} current (center) and with $I_{\mathrm{SAC}}+$ CONV term (right). Below each panel are reported the min, max and step in ms of the displayed map.

Effects of mechanical feedbacks on epicardial and endocardial waveforms.
We report finally in Figs. 9–11 the time evolution of the transmembrane (v) and
extracellular (u_e) potentials, intracellular calcium concentration ($[Ca^{2+}]_i$), active
tension (T_a), stretch along fiber (λ_l) and along fiber component of the Green –
Lagrange strain tensor (E_{ll}) at three selected points of the ventricular block denoted
by P_1, P_2, P_3 in Fig. 2.

The first point P_1 (Fig. 9) is located at the center of the epicardial surface and
presents an electrogram u_e with a positive T wave. The second point P_2 (Fig. 10)
is located at the apex of the epicardial surface and presents an electrogram u_e
with a biphasic T wave. The third point P_3 (Fig. 11) is located at the base of the
endocardial surface and presents an electrogram u_e with a negative T wave. As in
the previous figures, we have reported only the results concerning the simulations
without I_{SAC}, with I_{SAC} and with $I_{SAC} + CONV$. The time profile of the trans-
membrane potential v (also called action potential) exhibits a fast upstroke related
to the excitation phase followed by a plateau and recovery phase, while the time
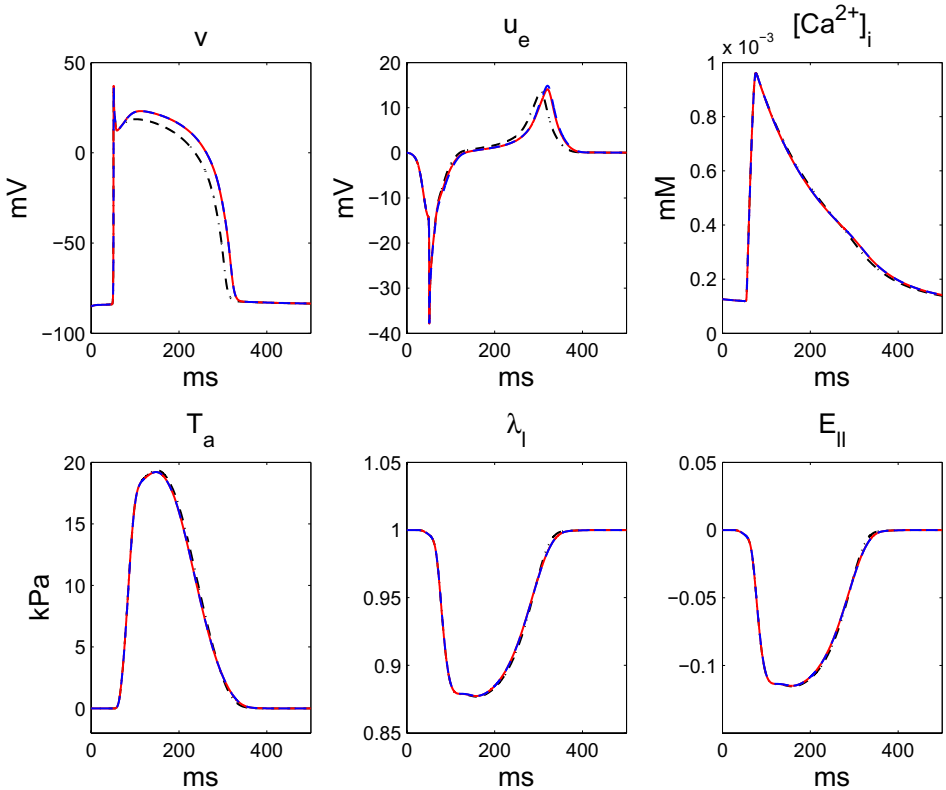profile of the extracellular potential u_e (also called electrogram) shows a first QRS

Fig. 9. (Color online) Waveforms at the center of the epicardial surface, without I_{SAC} current
(black, dashed-dot), with I_{SAC} current (red, continuous) and $I_{SAC} + CONV$ term (blue, dashed).
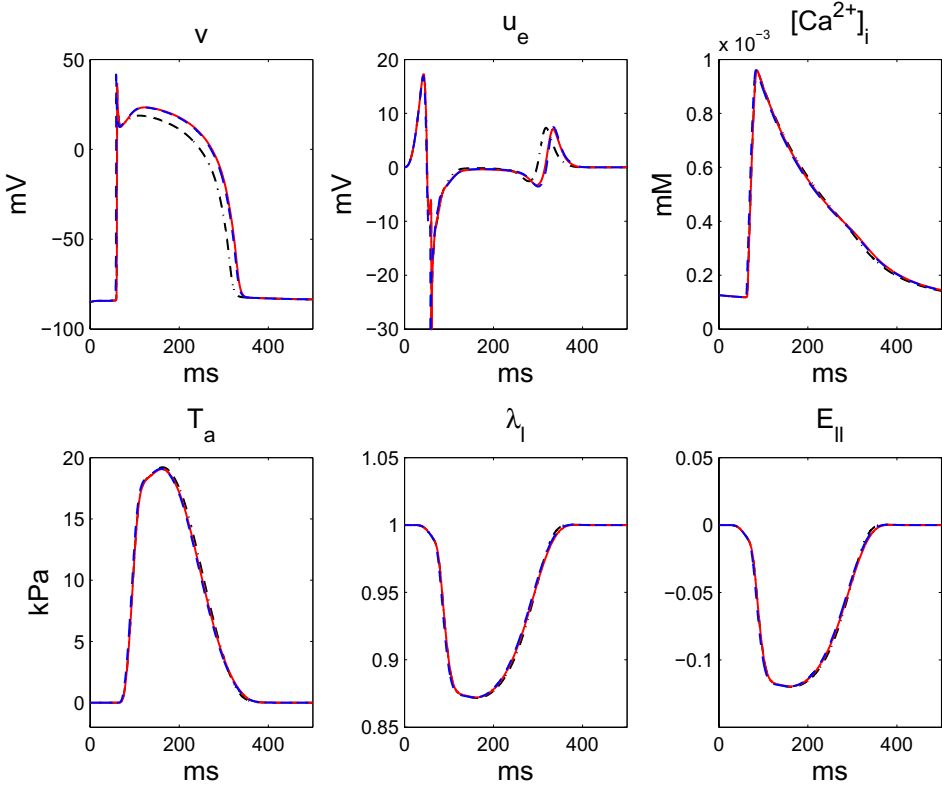
Fig. 10.   (Color online) Epicardial waveforms at the apex, without I_{SAC} current (black, dashed-dot), with I_{SAC} current (red, continuous) and $I_{SAC} + CONV$ term (blue, dashed).

complex related to the excitation phase, followed by a T wave associated to the recovery phase.

The different types of mechanical feedbacks do not modify significantly the main morphological features of the v and u_e waveforms, but they have a visible influence on the plateau and repolarization phases of v and on the T wave of u_e. The comparison of the epicardial waveforms in presence of I_{SAC} and of $I_{SAC} + CONV$ shows almost coincident profiles in agreement with the comparable APD dispersion previously observed at the epicardial level. The main difference on the v waveforms appears for the simulation without I_{SAC} due to an early repolarization downstream profile, i.e. a shift on the left of the profile yielding a shorter APD, while the main difference on the u_e waveform is an earlier T wave, with lower peak, always for the simulation without I_{SAC}. The other four mechanical waveforms at the epicardial locations P_1, P_2 exhibit negligible differences, which are a bit more visible in the waveforms associated with the endocardial base location P_3, i.e. the upper portion of the block which is one of latest activated region (Fig. 11) where a delay of the upstroke phase is observed for simulation without I_{SAC}.
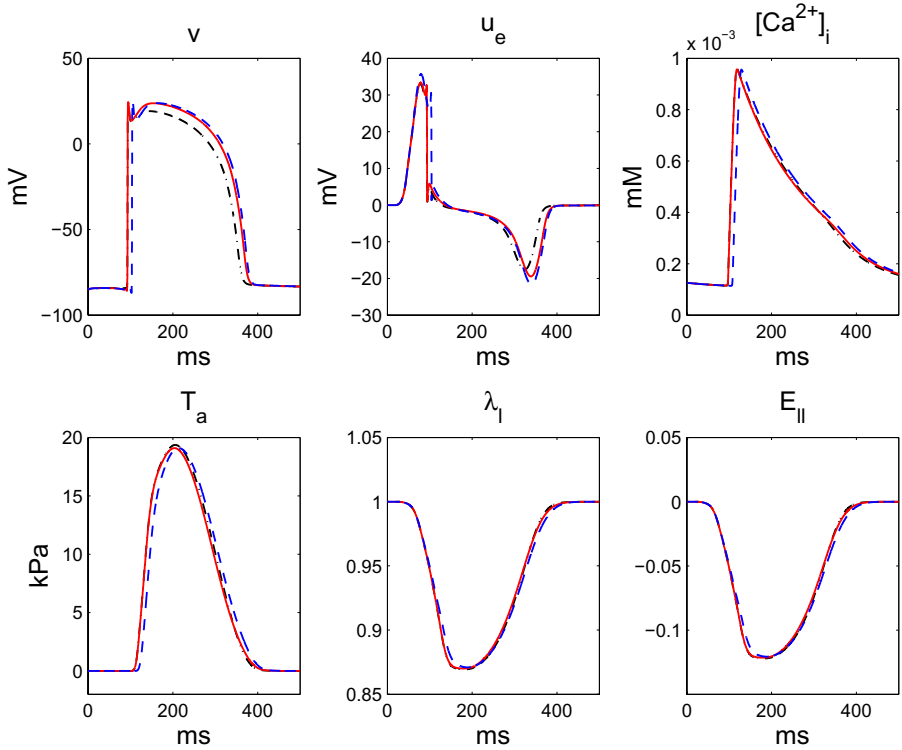
Fig. 11. (Color online) Endocardial waveforms at the base, without I_{SAC} current (black, dashed-dot), with I_{SAC} current (red, continuous) and $I_{\text{SAC}} + \text{CONV}$ term (blue, dashed).

5. Conclusions

In this work, we have developed a strongly coupled electro-mechanical model, where the Bidomain model is set on the deformed tissue configuration. When this model is properly re-written in the reference configuration, three mechanical feedbacks appear, and cardiac deformation affects the Bidomain model through: (i) the presence of the deformation gradient $\mathbf{F}$ in the conductivity coefficients, (ii) the presence of the deformation gradient $\mathbf{F}$ and the deformation rate $\mathbf{V}$ in the convective term $\mathbf{F}^{-T}\,\text{Grad}\,\widehat{v}\cdot\mathbf{V}$, (iii) the presence of the stretch λ in the ionic membrane current due to the stretch-activated current. We have simulated the electro-mechanical response of an insulated block of ventricular wall, fixed at the base and stimulated locally at the endocardial surface. In order to avoid masking the effects of mechanical feedbacks by the presence of heterogeneity of the cellular membranes, we have performed all simulations in a cardiac tissue with homogeneous cell membrane properties. Our results have shown that the mechanical feedbacks do not alter the pattern of the activation and repolarization sequences and the morphology of the transmembrane action potential and electrogram waveforms, while they strongly affect the action potential duration (APD) patterns. In particular, the I_{SAC} current prolongs the

APD of about 10–15 ms and the inclusion into the model of both I_{SAC} current and the convective term reduces the dispersion of repolarization of about 7% (from 139 to 129 ms) and increases the dispersion of APD about three times (from 13 to 45 ms). These effects indicate that mechanical feedbacks might influence arrhythmogenic mechanisms when combined with pathological substrates, particularly in presence of tissue heterogeneity, that should be investigated in future studies.

Acknowledgment

References

1. I. Adeniran, J. C. Hancox and H. Zhang, Effect of cardiac ventricular mechanical contraction on the characteristics of the ECG: A simulation study, *J. Biomed. Sci. Engrg.* **6** (2013) 47–60.
2. D. Ambrosi, G. Arioli, F. Nobile and A. Quarteroni, Electromechanical coupling in cardiac dynamics: The active strain approach, *SIAM J. Appl. Math.* **71** (2011) 605–621.
3. D. Ambrosi and S. Pezzuto, Active stress vs. active strain in mechanobiology: Constitutive issues, *J. Elast.* **107** (2012) 199–212.
4. B. Andreianov, M. Bendahmane, A. Quarteroni and R. Ruiz-Baier, Solvability analysis and numerical approximation of linearized cardiac electromechanics, preprint (2014), http://hal.archives-ouvertes.fr/hal-00865585.
5. S. Balay, K. Buschelman, W. D. Gropp, D. Kaushik, M. Knepley, L. Curfman McInnes, B. F. Smith and H. Zhang, PETSc users manual, Techincal Report ANL-95/11, Revision 3.3, Argonne National Laboratory (2012).
6. S. G. Campbell, E. Howard, J. Aguado-Sierra, B. A. Coppola, J. H. Omens, L. J. Mulligan, A. D. McCulloch and R. C. P. Kerckhoffs, Effect of transmurally heterogeneous myocyte excitation-contraction coupling on canine left ventricular electromechanics, *Exp. Physiol.* **94** (2009) 541–552.
7. V. Carapella, R. Bordas, P. Pathmanathan, M. Lohezic, J. E. Schneider, P. Kohl, K. Burrage and V. Grau, Quantitative study of the effect of tissue microstructure on contraction in a computational model of rat left ventricle, *PloS ONE* **9** (2014) e92792.
8. C. Cherubini, S. Filippi, P. Nardinocchi and L. Teresi, An electromechanical model of cardiac tissue: Constitutive issues and electrophysiological effects, *Progr. Biophys. Molec. Biol.* **97** (2008) 562–573.
9. P. Colli Franzone, L. Guerri and B. Taccardi, Modeling ventricular excitation: Axial and orthotropic effects on wavefronts and potentials, *Math. Biosci.* **188** (2004) 191–205.
10. P. Colli Franzone, L. F. Pavarino and S. Scacchi, A comparison of coupled and uncoupled solvers for the cardiac bidomain model, *ESAIM Math. Mod. Numer. Anal.* **47** (2013) 1017–1035.
11. P. Colli Franzone, L. F. Pavarino and S. Scacchi, *Mathematical Cardiac Electrophysiology*, Modeling, Simulation and Applications, Vol. 13 (Springer, 2014).
12. P. Colli Franzone, L. F. Pavarino and S. Scacchi, Parallel multilevel solvers for the cardiac electro-mechanical coupling, *Appl. Numer. Math.* **95** (2015) 140–153.

13. A. Collin, Analysie asymptotic en électrophysioloie cardiaque. application a la modelisation et à la modelélisation et à l'assimilation de données, Ph.D. thesis, Université Pierre et Marie Curie, Paris VI (2014).

14. J. Constantino, Y. X. Hu, A. C. Lardo and N. A. Trayanova, Mechanistic insight into prolonged electromechanical delay in dyssynchronous heart failure: A computational study, *Amer. J. Physiol. Heart Circ. Physiol.* **305** (2013) H1265–H1273.

15. K. D. Costa, J. W. Holmes and A. D. McCulloch, Modelling cardiac mechanical properties in three dimensions, *Philos. Trans. Roy. Soc. London A* **359** (2001) 1233–1250.

16. H. Dal, S. Göktepe, M. Kaliske and E. Kuhl, A fully implicit finite element method for bidomain models of cardiac electromechanics, *Comput. Meth. Appl. Mech. Engrg.* **253** (2013) 323–336.

17. B. L. de Oliveira, B. M. Rocha, L. P. S. Barra, E. M. Toledo, J. Sundnes and R. W. dos Santos, Effects of deformation on transmural dispersion of repolarization using in silico models of human left ventricular wedge, *Int. J. Num. Meth. Biomed. Engrg.* **29** (2013) 1323–1337.

18. T. S. E. Eriksson, A. J. Prassl, G. Plank and G. A. Holzapfel, Influence of myocardial fiber/sheet orientations on left ventricular mechanical contraction, *Math. Mech. Solids* **18** (2013) 592–606.

19. S. Göktepe and E. Kuhl, Electromechanics of the heart — A unified approach to the strongly coupled excitation-contraction problem, *Comput. Mech.* **80** (2010) 227–243.

20. J. M. Guccione, K. D. Costa and A. D. McCulloch, Finite element stress analysis of left ventricular mechanics in the beating dog heart, *J. Biomech.* **28** (1995) 1167–1177.

21. R. M. Gulrajani, *Bioelectricity and Biomagnetism* (Wiley, 1998).

22. V. Gurev, J. Constantino, J. J. Rice and N. A. Trayanova, Distribution of electromechanical delay in the heart: Insights from a three-dimensional electromechanical model, *Biophys. J.* **99** (2010) 745–754.

23. V. Gurev, T. Lee, J. Constantino, H. Arevalo and N. A. Trayanova, Models of cardiac electromechanics based on individual hearts imaging data: Image-based electromechanical models of the heart, *Biomech. Model Mechanobiol.* **10** (2011) 295–306.

24. V. E. Henson and U. M. Yang, BoomerAMG: A parallel algebraic multigrid solver and preconditioner, *Appl. Numer. Math.* **41** (2002) 155–177.

25. G. A. Holzapfel, *Nonlinear Solid Mechanics*: *A Continuum Approach for Engineering* (Wiley, 2000).

26. G. A. Holzapfel and R. W. Ogden, Constitutive modelling of passive myocardium. A structurally-based framework for material characterization, *Philos. Trans. Roy. Soc. London A* **367** (2009) 3445–3475.

27. J. D. Humphrey, *Cardiovascular Solid Mechanics, Cells, Tissues and Organs* (Springer, 2001).

28. P. J. Hunter, A. D. McCulloch and H. E. D. J. ter Keurs, Modelling the mechanical properties of cardiac muscle, *Progr. Biophys. Molec. Biol.* **69** (1998) 289–331.

29. X. Jie, V. Gurev and N. A. Trayanova, Mechanisms of mechanically induced spontaneous arrhythmias in acute regional ischemia, *Circ. Res.* **106** (2010) 185–192.

30. J. P. Keener and J. Sneyd, *Mathematical Physiology* (Springer, 2008).

31. R. H. Keldermann, M. P. Nash, H. Gelderblom, V. Y. Wang and A. V. Panfilov, Electromechanical wavebreak in a model of the human left ventricle, *Amer. J. Physiol. Heart Circ. Physiol.* **299** (2010) H134–H143.

32. R. H. Keldermann, M. P. Nash and A. V. Panfilov, Modeling cardiac mechanoelectrical feedback using reaction–diffusion–mechanics systems, *Physica D* **238** (2009) 1000–1007.

33. R. C. P. Kerckhoffs, P. H. M. Bovendeerd, J. C. S. Kotte, F. W. Prinzen, K. Smits and T. Arts, Homogeneity of cardiac contraction despite physiological asyncrony of depolarization: A model study, *Ann. Biomed. Engrg.* **31** (2003) 536–547.

34. R. C. P. Kerckhoffs, S. N. Healy, T. P. Usyk and A. D. McCulloch, Computational methods for cardiac electromechanics, *Proc. IEEE* **94** (2006) 769–783.

35. R. C. P. Kerckhoffs, M. Neal, Q. Gu, J. B. Bassingthwaighte, J. H. Omens and A. D. McCulloch, Coupling of 3d finite element method of cardiac ventricular mechanic to lmped systems models of the systemica and pulmonic circulation, *Ann. Biomed. Engrg.* **35** (2007) 1–18.

36. R. C. P. Kerckhoffs, J. H. Omens, A. D. McCulloch and L. J. Mulligan, Ventricular dilation and electrical dyssynchrony synergistically increase regional mechanical nonuniformity but not mechanical dyssynchrony: A computational model, *Circ. Heart Fail.* **3** (2010) 528–536.

37. S. Land, S. A. Niederer, J. M. Aronsen, E. K. S. Espe, L. L. Zhang, W. E. Louch, I. Sjaastad, O. M. Sejersted and N. P. Smith, An analysis of deformation-dependent electromechanical coupling in the mouse heart, *J. Physiol.* **590** (2012) 4553–4569.

38. I. J. LeGrice, B. H. Smaill, L. Z. Chai, S. G. Edgar, J. B. Gavin and P. J. Hunter, Laminar structure of the heart: Ventricular myocyte arrangement and connective tissue architecture in the dog, *Amer. J. Physiol. Heart Circ. Physiol.* **269** (1995) H571–H582.

39. J. E. Marsden and T. J. R. Hughes, *Mathematical Foundations of Elasticity* (Dover Publications, 1994).

40. M. P. Nash and P. J. Hunter, Computational mechanics of the heart from tissue structure to ventricular function, *J. Elast.* **61** (2000) 113–141.

41. M. P. Nash and A. V. Panfilov, Electromechanical model of excitable tissue to study reentrant cardiac arrhythmias, *Progr. Biophys. Molec. Biol.* **85** (2004) 501–522.

42. J. S. Neu and W. Krassowska, Homogenization of syncytial tissues, *CRC Crit. Rev. Biomed. Engrg.* **21** (1993) 137–199.

43. D. Nickerson, N. Smith and P. Hunter, New developments in a strongly coupled cardiac electromechanical model, *Europace* **7** (2005) S118–S127.

44. S. A. Niederer and N. P. Smith, A mathematical model of the slow force response to stretch in rat ventricular myocites, *Biophys. J.* **92** (2007) 4030–4044.

45. S. A. Niederer and N. P. Smith, An improved numerical method for strong coupling of excitation and contraction models in the heart, *Progr. Biophys. Molec. Biol.* **96** (2008) 90–111.

46. F. Nobile, A. Quarteroni and R. Ruiz-Baier, An active strain electromechanical model of cardiac tissue, *Int. J. Num. Meth. Biomed. Engrg.* **28** (2012) 52–71.

47. S. Osher and R. Fedkiw, *Level Set Methods and Dynamic Implicit Surfaces*, Applied Mathematical Sciences, Vol. 153 (Springer, 2003).

48. P. J. Pathmanathan and J. P. Whiteley, A numerical method for cardiac mechano-electric simulations, *Ann. Biomed. Engrg.* **37** (2009) 860–873.

49. S. J. Pathmanathan, P. J. Chapman, D. J. Gavaghan and J. P. Whiteley, Cardiac electromechanics: The effect of contraction model on the mathematical problem and accuracy of the numerical scheme, *Quart. J. Mech. Appl. Math.* **63** (2010) 375–399.

50. L. F. Pavarino and S. Scacchi, Multilevel additive Schwarz preconditioners for the Bidomain reaction–diffusion system, *SIAM J. Sci. Comput.* **31** (2008) 420–443.

51. M. Pennacchio, G. Savaré and P. Colli Franzone, Multiscale modeling for the bioelectric activity of the heart, *SIAM J. Math. Anal.* **37** (2006) 1333–1370.

52. R. Plonsey and D. Heppner, Consideration of quasi-stationarity in electrophysiological systems, *Bull. Math. Biophys.* **29** (1967) 657–664.

53. E. W. Remme, M. P. Nash and P. J. Hunter, Distributions of myocyte stretch, stress and work in models of normal and infarcted ventricles, in *Cardiac Mechano-Electric Feedback and Arrhythmias*: *From Pipette to Patient*, eds. P. Kohl, F. Sachse and M. R. Franz (Saunders-Elsevier, 2005), pp. 389–391.

54. S. Rossi, T. Lassila, R. Ruiz-Baier, A. Sequeira and A. Quarteroni, Thermodynamically consistent orthotropic activation model capturing ventricular systolic wall thickening in cardiac electromechanics, *Eur. J. Mech. A-Solids* **48** (2014) 129–142.

55. S. Rossi, R. Ruiz-Baier, L. F. Pavarino and A. Quarteroni, Orthotropic active strain models for the numerical simulation of cardiac biomechanics, *Int. J. Num. Meth. Biomed. Engrg.* **28** (2012) 761–788.

56. J. Sainte-Marie, D. Chapelle, R. Cimrman and M. Sorine, Modeling and estimation of cardiac electromechanical activity, *Comput. Struct.* **84** (2006) 1743–1759.

57. S. Scacchi, A hybrid multilevel Schwarz method for the bidomain model, *Comput. Meth. Appl. Mech. Engrg.* **197** (2008) 4051–4061.

58. H. Schmid, M. P. Nash, A. A. Young and P. J. Hunter, Myocardial material parameter estimation—A comparative study of simple shear, *J. Biomech. Engrg.* (*Trans. Asme*) **128** (2006) 742–750.

59. J. Sundnes, S. Wall, H. Osnes, T. Thorvaldsen and A. D. McCulloch, Improved discretisation and linearisation of active tension in strongly coupled cardiac electromechanics simulations, *Comput. Meth. Biomech. Biomed. Engrg.* **17** (2014) 604–615.

60. K. H. W. J. Ten Tusscher, D. Noble, P. J. Noble and A. V. Panfilov, A model for human ventricular tissue, *Amer. J. Phys. Heart. Circ. Physiol.* **286** (2004) H1573–H1589.

61. T. P. Usyk, I. J. LeGrice and A. D. McCulloch, Computational model of three-dimensional cardiac electromechanics, *Comput. Visual. Sci.* **4** (2002) 249–257.

62. T. P. Usyk, R. Mazhari and A. D. McCulloch, Effect of laminar orthotropic myofiber architecture on regional stress and strain in the canine left ventricle, *J. Elast.* **61** (2000) 143–164.

63. F. J. Vetter and A. D. McCulloch, Three-dimensional stress and strain in passive rabbit left ventricle: A model study, *Ann. Biomed. Engrg.* **28** (2000) 781–792.

64. S. T. Wall, J. M. Guccione, M. B. Ratcliffe and J. S. Sundnes, Electromechanical feedback with reduced cellular connectivity alters electrical activity in an infarct injures left ventricle: A finite element model study, *Amer. J. Physiol. Heart Circ. Physiol.* **302** (2012) H206–H214.

65. J. P. Whiteley, M. J. Bishop and D. J. Gavaghan, Soft tissue modelling of cardiac fibres for use in coupled mechano-electric simulations, *Bull. Math. Biol.* **69** (2007) 2199–2225.